Delft University of Technology

MSc Thesis
CIE5060-09

# Overturning Strength of the Sub-Polar Gyre in the North Atlantic Ocean, within the GLORYS12 reanalysis model

*Authors:*
David Johannes Oldenhuis (4453816)

*Supervisors:*
Prof. Dr. C.A. Katsman
Dr. S.R. de Roode

November 24, 2023

**Abstract**

The Earth's climate is changing, due to global warming, impacting the ocean circulation around the world. As the ocean circulation distributes large amounts of energy around the world, this can alter climate drastically if changed. The Atlantic Meridional Overturning Circulation (AMOC) is a fundamental ocean component to comprehend climate change and further investigation enhances our capacity to predict it. The AMOC plays a pivotal role in regulating the ocean heat transport within the North Atlantic Ocean, influencing the climates of North America and Europe. This study centers its attention on the Sub-Polar Gyre (SPG), a critical region where the AMOC activity peaks. Within this region, this study aims to get a better understanding of the overturning dynamics of the SPG, on a seasonal and annual time scale. To achieve this, the reanalysis model GLORYS12 is used, which offers a detailed simulation of ocean dynamics spanning the period from 1993 to 2020. With its high-resolution, eddy-resolving capabilities, GLORYS12 is particularly well-suited for capturing the nuanced small-scale overturning processes associated with the AMOC. From these model data, the overturning is calculated from alongstream changes in boundary current transport divided in density classes. The analysis is performed for the entire SPG by dividing it into its major basins: the Iceland Basin, Irminger Sea, and Labrador Sea. Subsequently, the boundary currents of the SPG are further subdivided into seventeen individual segments, providing insights into how overturning dynamics vary along the SPG. The results reveal that the mean overturning strength in the SPG for 1993-2020 is 23.8 Sverdrups ($10^6$ $m^3/s$ (Sv)). The distribution in overturning strength between the basins is 41%, 29%, and 30% for the Iceland Basin, Irminger Sea, and Labrador Sea respectively. Furthermore, the results shows overturning occurs at increasingly higher densities, the further west you go. Each basin displays a pronounced seasonal pattern, with maximum overturning occurring in March and the minimum in September. On an inter-annual time scale, the overturning strength in both the Iceland Basin and Irminger Sea exhibits a decreasing trend of -0.04 and -0.02 Sv/year respectively, whereas the Labrador Sea has an increasing trend of 0.02 Sv/year over 1993-2020. A further division in shorter segments yields large spatial differences in overturning, both in overall strength and the distribution over density classes. However, these outcomes are less robust as flows are highly variable and numerical errors associated with the overturning calculations become more prominent. This also raises questions about the reliability of the assessment of overturning along segments from observations to determine the local overturning dynamics. In conclusion, this study leverages GLORYS12 for a detailed basin and segmented analyses to offer a comprehensive understanding of the AMOC within the SPG. The findings provide valuable insights into the AMOC's long-term behavior, seasonal variations, annual trends, and high spatial variability. Using this increased understanding, future research can improve on why the AMOC behaves in the observed way, by analyzing the overturning dynamics sensitivity to oceanic and atmospheric conditions.

# 1 Introduction

Investigating climate change is crucial for understanding its impacts on our environment, societies, and economies and for developing effective strategies to mitigate its adverse effects and adapt to a changing world. The climate predictions from the IPCC still have a high range of uncertainty (Core Writing Team, H. Lee and J. Romero (eds.), 2023). The world's oceans heavily influence Earth's climate and are one of the causes of this uncertainty.

In the oceans are a multitude of currents transporting heat all around the world. Heat from around the equator is transported via the surface currents towards higher latitudes, with a return flow of colder and deeper currents. This circulation is called the thermohaline circulation (THC) of which a sketch is shown in figure 1). Here the red arrows represent the warm surface currents and the blue arrows represent the colder and deeper currents. Density differences in the ocean drive the THC. Mainly, these density differences are caused by temperature differences in the water. The blue currents flow in a deeper part of the ocean, compared to the red currents, because of the density difference of the water. These flow independently of each other in most parts of the world. However, a connection is made between the surface and deep currents at high latitudes in the Atlantic Ocean. At low altitudes, the atmosphere is heating the surface, creating low-density waters. At high altitudes the water is cooled down, increasing its density. In figure 1 this is indicated by the circles marked 'heat released to air' in the North Atlantic Ocean. The return currents going south, indicated by the blue arrows, consist of high-density waters.

Additionally, there is also a wind-driven part influencing the ocean currents. The trade winds create large circulating currents, called gyres, dictating the flow in the oceans major areas.

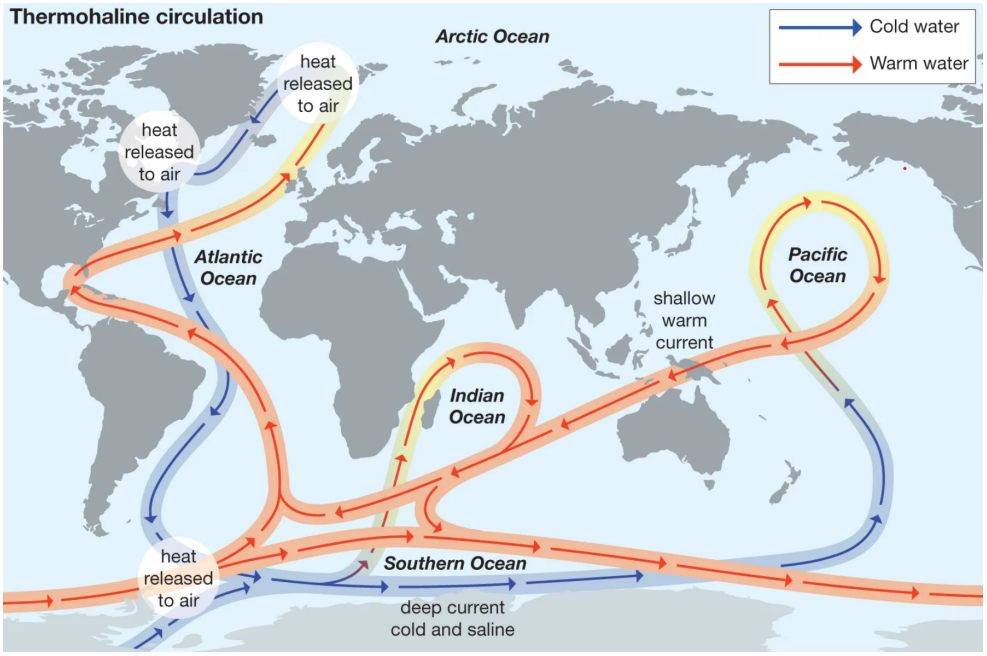


Figure 1: Schematic representation of the thermohaline circulation. Red arrows are the relative warm and low density surface currents and the blue arrows are the relative cool and high density deep currents (Britannica, 2023)

.

One of these areas is the Sub-Polar Gyre (SPG) in the North Atlantic Ocean. The SPG is a gyre, with water flowing counter clockwise as depicted in figure 2. In the figure the major currents of the SPG are shown. Here the North Atlantic Currents (NAC) depicts the warm incoming water from low latitudes, which was indicated by the red arrow in the North Atlantic Ocean in figure 1. A part of this water continious as the Irminger Current (IC), which flows to the South of Iceland and is then joined by the East Greenland Current (EGC) along the east coast of Greenland. This water flows around Greenland and continious as the Labrador Current (LC). Lastly, a part of the Labrador Current joins back up with the NAC and the IC in the east and another part in the west flows southward.

Along the SPG a so-called overturning occurs, where low density surface currents are transformed into high density deep currents (Desbruyères et al., 2020; Lozier et al., 2017). The Atlantic Meridional Overturning Circulation (AMOC) is defined as the total overturning in the SPG, determined over the entire width of the ocean basin. The strength of the AMOC is determined by the transport difference between relatively low density waters flowing northward and higher density waters flowing southward. This strength is often depicted in Sverdrups (Sv), which is $10^6$ $m^3$ per second. The latest observations show the AMOC strength has been between 21.1 and 12.3 Sv over the period 2014-2020 (Fu et al., 2023).

The IPCC reported an expected decrease of the AMOC strength of about 5 Sverdrup in 2100, mainly caused by a freshening of the surface waters due to ice melt over Greenland and increased precipitation over the northern seas (Core Writing Team, H. Lee and J. Romero (eds.), 2023). This decrease in the AMOC strength can result in increased sea level and temperature rise along North America, slower warming in Europe, and increased intensity storms in the North Atlantic. A better understanding of the processes governing the AMOC is needed to predict these future changes.

Historically, models have been used to investigate the AMOC. These models had a low spatial resolution of 1 degree and suggested the AMOC is predominantly caused by overturning in the Labrador Sea in the West of the SPG (reference). However, new insights are gained by recent studies using new observations from the Overturning in the Subpolar North Atlantic Program (OSNAP) by, among others, Holliday et al. (2018), Jean-Michel et al. (2021), Johnson et al. (2019), Chafik et al. (2022), Roussenov et al. (2022), and Koman et al. (2022). Most importantly, the primary factor in the overturning in the North Atlantic was previously thought to be the Labrador Sea. Still, these studies show the eastern part of the SPG (i.e. Iceland Basin and Irminger Sea) contributes up to 7 times more to the overturning as the Labrador Sea. This indicates the old models simulate the overturning poorly.

One of the issues models face is the small scale of the eddies in the ocean. In the SPG, water is transported along the boundary currents around the sub-basins in the North Atlantic. Water can gradually become more dense within the boundary currents due to heat loss to the atmosphere (Brüggemann and Katsman, 2019). In addition, in regions with high eddy activity, water can be transported to the interior of the sub-basins, where mixing with the deeper layers can occur, called deep convection (Brüggemann and Katsman, 2019), (Bower et al., 2019) and (Georgiou et al., 2021). Moreover, the eddy activity also allows water to mix locally within the boundary current to greater depths (Brüggemann and Katsman, 2019). These eddies have a spatial scale smaller than 10 kilometers, making it impossible for models with a lower resolution to simulate them (Danek et al., 2023). New high-resolution models, like the GLORYS12 reanalysis model, with a spatial resolution of about 5 km in the SPG (Jean-Michel et al., 2021), do have the capacity to simulate eddy formation, which enables a more detailed study of the high eddy activity zones.

This study aims to gain more insight in the overturning along the main currents of the subpolar gyre in the North Atlantic Ocean, using the recent GLORYS12 reanalysis model. First, the physics governing the currents and overturning in the SPG are presented in section 2, where first

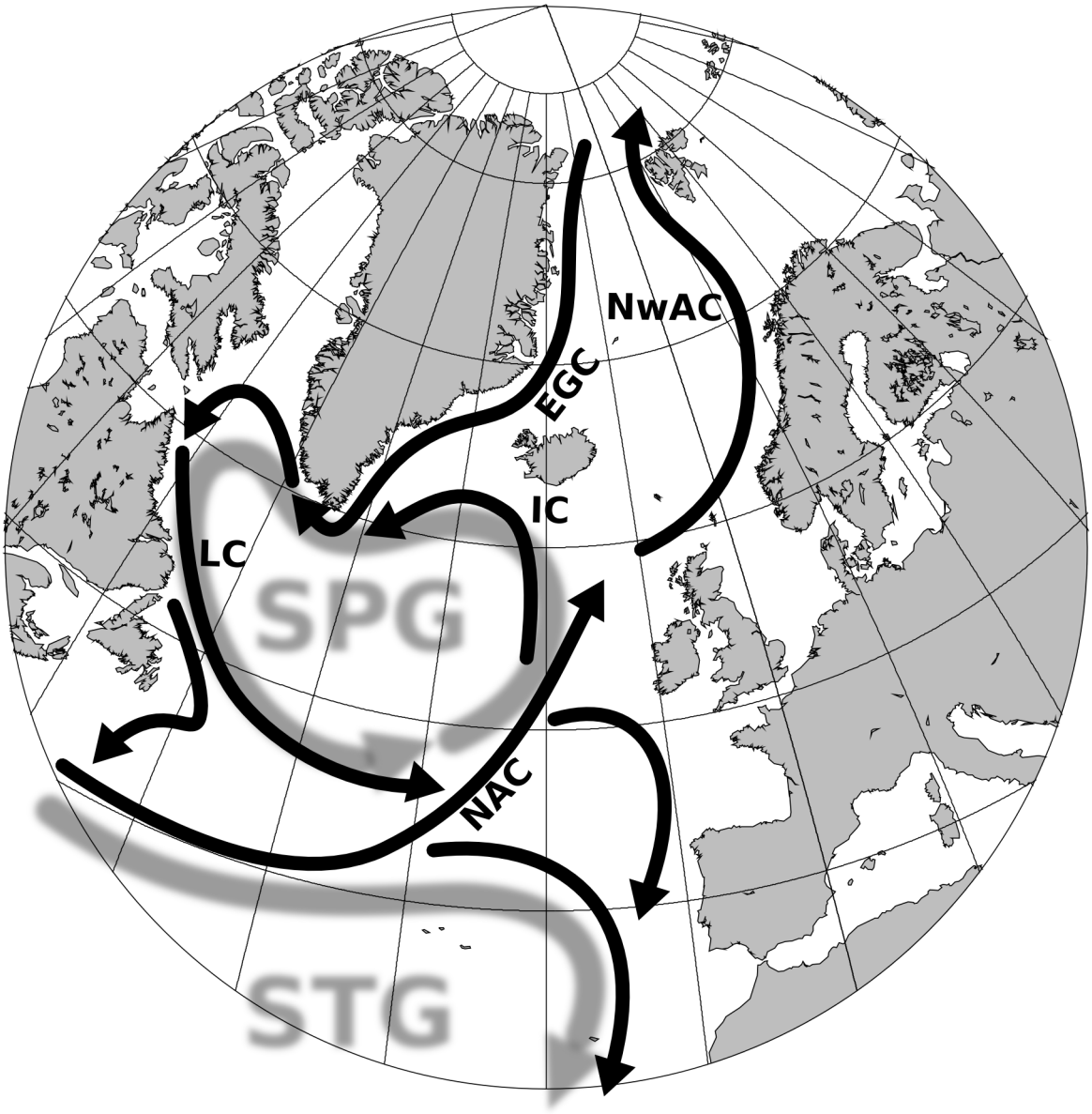


Figure 2: Schematic of the North Atlantic Ocean, with its major currents. In gray the Sub-Polar Gyre (SPG) is indicated as a counter clockwise flowing gyre, with in the East incoming water from the North Atlantic Current (NAC) and in the West a current leaving the gyre going Southwards. The SPG consists here of the Irminger Current (IC), which is joined by the East Greenland Current (EGC), transforms into the Labrador Current (LC). The Norwegian Atlantic Current (NwAC) is the part of the NAC that flows Northward, instead of flowing through the SPG.

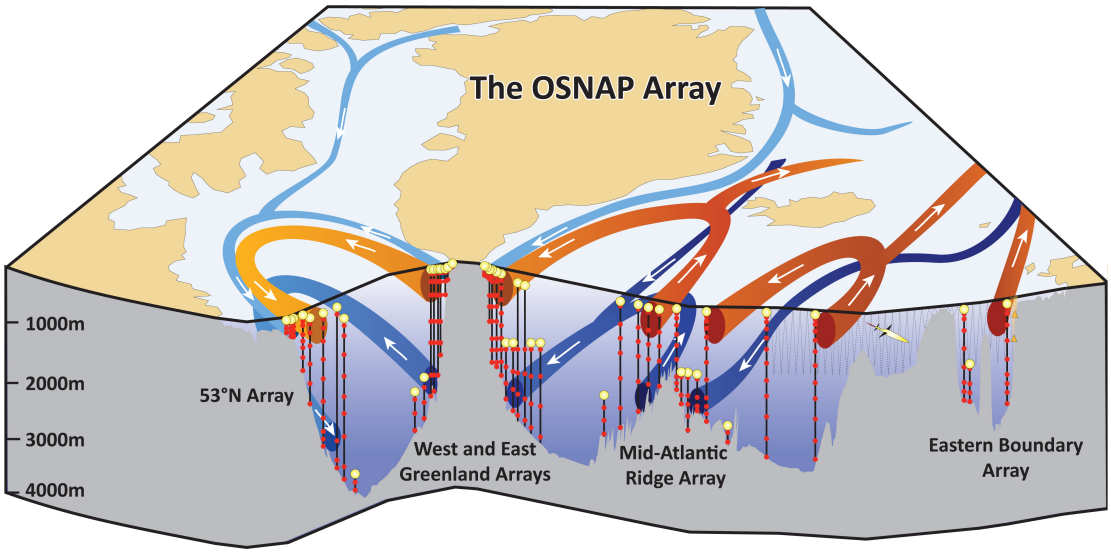


Figure 3: Schematic of the Sub-Polar Gyre (SPG) with its main currents presented by OSNAP (2023). The water increases in density from red to yellow to blue. The green currents consist of cold fresh melt water from the polar region. Currents depicted are: North Atlantic Current (NAC), East Reykjanes Ridge Current (ERRC), Irminger Current (IC), East Greenland Current (EGC), West Greenland Current (WGC) and Labrador Current (LC)

the currents are explained in section 2.a. Next, the process of convection is explained (section 2.b) and then the overturning processes are explained (section 2.c). This is followed by the research questions in section 2.d. Here the direction of the study is explained. Next, the methodology is outlined in section 3, where the model GLORYS12 is described and the overturning calculations are explained. From the method the results are presented in section 4. Here, answers are given to how strong the overturning is in the SPG, the time dependency and where in the SPG the overturning is most dominant. Lastly, conclusions are presented and discussed in section 5.

# 2 Physics of the Sub-Polar Gyre

This section explains the main currents of the SPG and the overturning processes. The SPG receives relatively warm and saline waters from the subtropical gyre along the North Atlantic Current (NAC). From the NAC it splits into different surface currents. These waters are densified within the SPG and form the North Atlantic Deep Waters, which are cooler and less saline, explained in section 2.a. A main process causing the densification is convection (section 2.b) and the overall process is called overturning, futher explained in section 2.c. Section 2.d presents the research questions.

## 2.a The boundary current of the SPG

The Sub-Polar Gyre (SPG) flows through multiple sub-seas of the North Atlantic Ocean: the Iceland Basin (IB), Irminger Sea (IRS) and the Labrador Sea (LS) (figures 4, 5 and 6). There are many currents distinguishable within the SPG. Broadly speaking, the currents can be sub-divided into three layers based on potential density $\sigma_0$ according to Daniault et al. (2016). $\sigma_0$ is defined as the density of water when raised adiabatically to the surface. This means heat and salinity are preserved, but the effects of pressure on the density are negated. $\sigma_0$ is reported as $\sigma_0$ - 1000 kg/m$^3$, because the range of $\sigma_0$ is 1027 - 1028 kg/m$^3$. The three layers are the surface layer ($\sigma_0 > 27.50$ kg/m$^3$), intermediate layer ($\sigma_0 = 27.50$ - 27.80 kg/m$^3$) and the deep layer ($\sigma_0 > 27.80$ kg/m$^3$) First the surface layer (figure 4), which are the red to yellow currents, originating from the North Atlantic Current (NAC), and the green currents, which consist of cold fresh meltwater from the icecaps and sea ice from the Arctic. The intermediate layer (figure 5) consists of the purple currents. They are mostly formed in the Labrador Sea and the Irminger Sea. The deepest layer, the dark blue currents, have their origin from the Arctic Seas (figure 6). The currents flow around three different basins: The Iceland Basin, the Irminger Sea, and the Labrador Sea. The currents experience a general densification from east to west, because of atmospheric cooling at the surface called shallow convection (section 2.b). In the centre of the three basins of the SPG, there is almost zero velocity. Here, the circumstances are such that deep convection can occur, allowing water to mix to great depths and increase in potential density (section 2.b).

## 2.b Convection

In this section convection is introduced, which plays an important part in the overturning. This will be elaborated in section 2.c, where the overturning is attributed to three distinct processes, which are individually explained.

Convection, or vertical mixing, is a process based on density differences in the water. The ocean is generally structured with low density waters at the surface and increasingly higher density water with increasing depth (figure 7a) , indicated by the increasingly darker blue. In this state, the ocean is in hydrostatic balance, with minimal convection. When the surface waters are cooled by the atmosphere, the density of the surface waters increases, creating an imbalance hydrostatically (figure 7b). The surface water then mixes vertically with the water below, due to gravity, creating a mixed layer (Stewart, 2008; Paquin et al., 2016). In the mixed layer, the density is constant and water can mix freely (figure 7c). This is called convection.

In this study, convection is further subdivided into shallow and deep convection. Shallow convection occurs at the surface, reaching down to 100 meters, and is most dominantly forced by the temperature difference between the surface water and the atmosphere and can occur anywhere in the ocean as long as there is a temperature difference.

Deep convection can reach depths down to 2000 meters but does not always occur (Jong et al.,

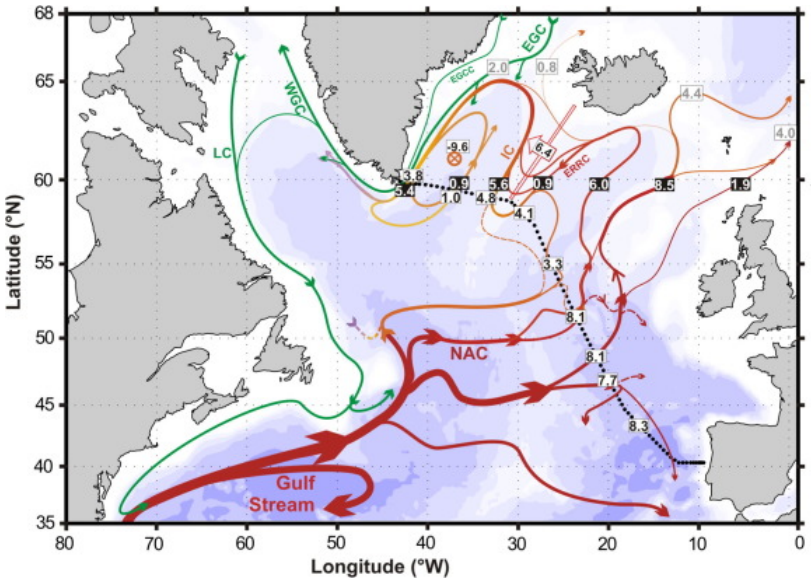


Figure 4: Schematic of the surface currents of the SPG (Daniault et al., 2016) with density $\sigma >$ 27.50 kg/m$^3$. Currents increase in density from red to yellow. The green currents are fresh melt waters. Numbers in black on white, grey on white and white on black are transport of the respective currents in Sverdrups from different studies presented by Daniault et al. (2016). Currents present are: North Atlantic Current (NAC), East Reykjanes Ridge Current (ERRC), Irminger Current (IC), East Greenland Current (EGC), East Greenland Coastal Current (EGCC), West Greenland Current (WGC), Labrador Current (LC).

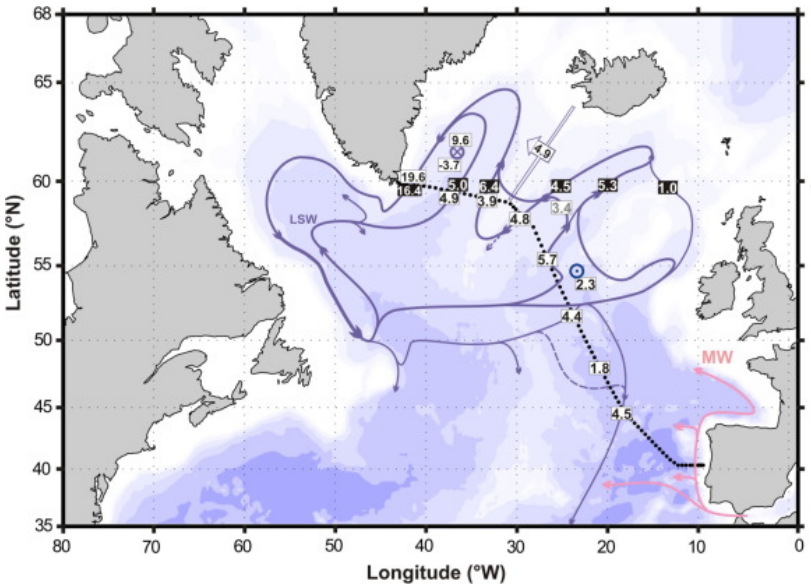


Figure 5: Schematic of the intermediate (or Labrador Sea Water (LSW)) currents of the SPG with a potential density $\sigma_0$ = 27.50 - 27.80 kg/m$^3$(Daniault et al., 2016).

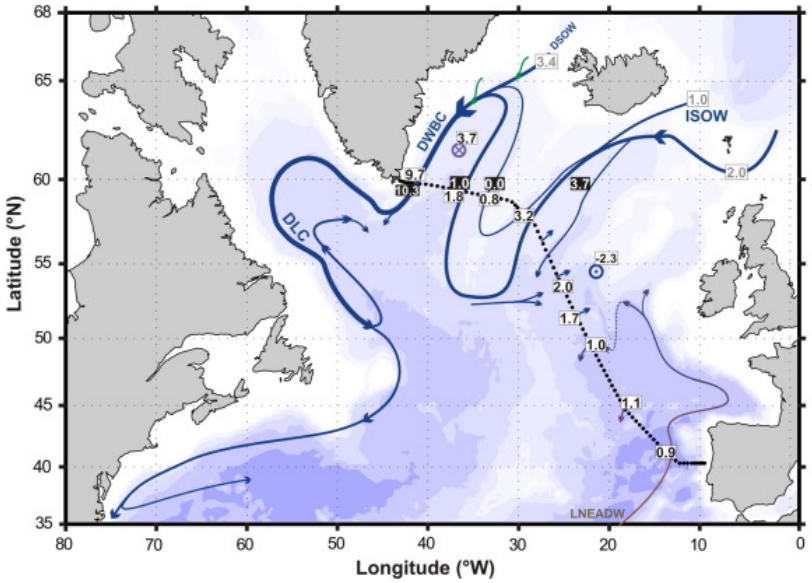


Figure 6: Schematic of the deep currents of the SPG by (Daniault et al., 2016) with a density of $\sigma > 27.80$ kg/m$^3$. The currents in the deep layer are: Iceland-Scotland Overflow Water (ISOW), Denmark-Strait Overflow Water (DSOW), Deep Western Boundary Current (DWBC), Deep Labrador Current (DLC).

2012). First, the density difference between surface and deep waters must be as low as possible, so the water column is close to hydrostatic instability. This occurs in regions where surface waters are nearly freezing, so the density is already relatively high at the surface. The surface density can be further increased by brine rejection when sea ice forms, increasing the salinity and thus density of the water. Then, a cyclonic boundary current, which creates Ekman suction, decreases the hydrostatic stability. The Irminger and Labrador Sea in the SPG have these conditions, with relative cold and dense surface waters and a cyclonic boundary current. Figure 8 shows a schematic of the Irminger or Labrador Sea. Figure panel (a) is a top view, where the blue arrows represent the boundary current of the basin and the white arrows the cyclonic rotation in the basin's center. Panel (b) shows the cross-section between I-II, where the color gradient represents the density of the water and the purple arrows represent the Ekman suction and Ekman surface transport. The density contour lines (or isopycnals), which are lines of constant density, curve upward in the center of the basin. This creates a deep mixed layer (panel (c)), where deep convection occurs.

## 2.c Overturning Processes

The overturning in the SPG is characterized by the northward transport of warm surface waters and the southward transport of cold deep waters. There are three distinct overturning processes within the SPG (Brüggemann and Katsman, 2019), which are discussed in this section. The first two are based on deep and shallow convection and the third is a water exchange between the SPG and the Arctic Seas.

Starting with the processes based on convection, figure 9 shows again a schematic of a sub-basin in the SPG. The cyclonic boundary current is shown here in 2D with the inflow on the right and outflow left and the blue gradient representing the water's density. At the inflow, there is a strong

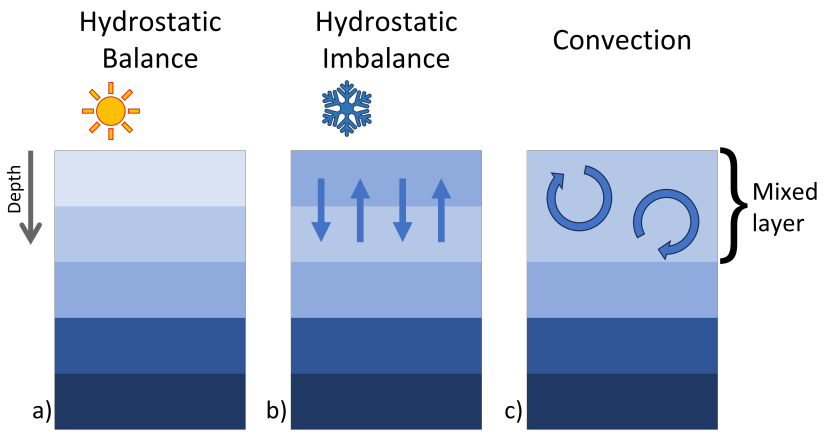


Figure 7: (a) Schematic of a water column in hydrostatic balance in the ocean. When the atmospheric temperature is lower than the surface water, it cools down the surface water, increasing its density. (b) If the surface layer becomes denser than the layer below, then the water column is in hydrostatic imbalance. (c) This results in convection.

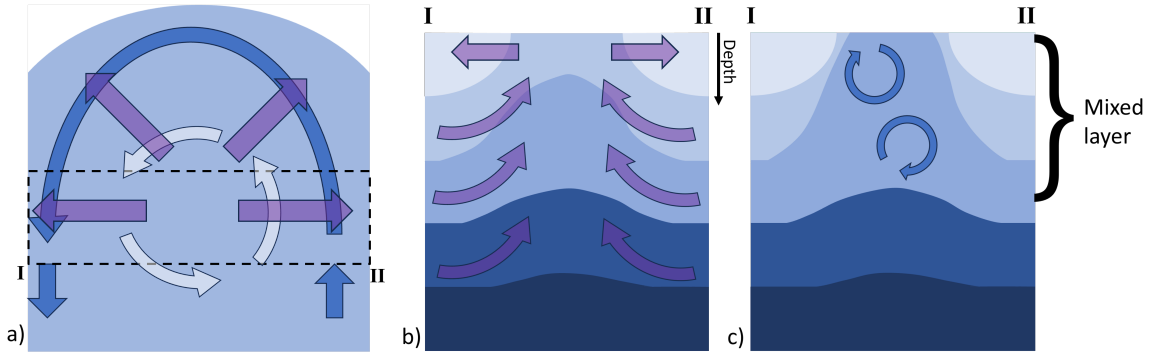


Figure 8: (a) A sketch of Ekman suction in a basin of the SPG. The boundary current has a cyclonic direction. (b) This generates Ekman suction in the basin's center, resulting in upward curving isopycnals. (c) Combined with a cold atmosphere, this leads to a deep mixed layer.

low density flow, indicated by the big red arrow, and a weak high density flow, indicated by the small purple arrow. The outflow consists of high density water, indicated by the big purple arrow. The overturning of the boundary current happens in two ways.

Process one is based on the deep convection occurring in the basin's interior. This process is characterized by an offshore eddy-driven transport of low density water (1a) and an onshore return flow of high density water (1c). In the interior (1b), deep convection occurs as in figure 8 (Brüggemann and Katsman, 2019). The low density offshore transport mixes with the high density interior. The return onshore return current has the interior's density and thus flows back into the boundary current at larger depth, because this flow has to follow the isopycnals. The net result is an overall higher density boundary current. Two known locations are the North-Eastern area of the Labrador Sea (Georgiou et al., 2021) and the Western area of the Irminger Sea (Jong et al., 2012; Bras et al., 2018; Holliday et al., 2018).

The second convection-based overturning process is shallow convection within the boundary current (2). Due to heat loss to the atmosphere, the surface layer increases in density. This enables shallow convection as depicted in figure 7.

The third process is the overflow currents. These currents flow over the Greenland-Scotland Ridge, with a northward flowing low density surface current towards the Nordic and Arctic Seas and a southward flowing high density deep current (figure 4, 5 and 6). In the Nordic Seas the northward flowing water is cooled down and salinified, due to brine rejection, creating extremely high density waters. As the return flows over the Greenland-Scotland Ridge it continues as the deep boundary current in the SPG, flowing close to the ocean floor (figure 6). This exchange with the Nordic Seas has a net overturning effect in the boundary currents of the SPG, with a decrease of low density waters and an increase of high density waters. Next to that, there is a low density current coming from the arctic and the Hudson-Davis Strait consisting of melt water (green current figure 4). This does not contribute to the overturning but will influence the results, by introducing low density water to the Irminger and Labrador Seas.

Overall, the SPG is an area where the boundary currents are overturned from warm surface currents to cold deep currents. There are three different processes governing the overturning: shallow convection within the boundary current caused by heat loss to the atmosphere; lateral transport exchange with the interior of a sub-basin, where deep convection can occur; and overflow currents flowing into the SPG.

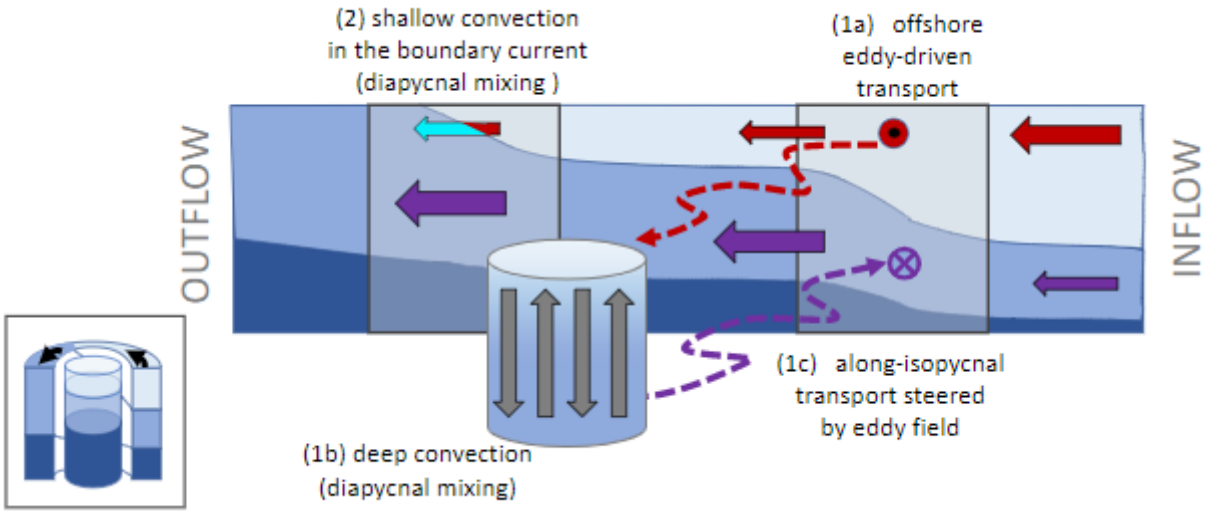


Figure 9: Schematic view of the two overturning processes in a ocean basin of the SPG (Brüggemann and Katsman, 2019). At 1a low density water is transported towards the interior of the basin. In the interior (1b) deep convection occurs and the water is densified. 1c represents the return flow of the denser water towards a lower part of the boundary current with the same density (low density red currents and high density purple currents). 2 represents the shallow convection within the boundary current itself (from red to blue).

## 2.d Research Questions

The overturning processes are now defined, but the question remains: where exactly do they occur in the SPG and how do they vary spatially and temporally? This study aims to answer this overarching question by addressing the following research questions:

1. How strong is the long-term mean overturning strength in the entire Sub-Polar Gyre (SPG) and what is the distribution of overturning strength between its major basins and overflow regions?

2. How does its monthly climatology vary for the entire SPG and its major basins and overflow regions?

3. How does the annual mean overturning strength change over time for the entire SPG and its major basins and overflow regions?

4. How do the outcomes of questions 1 and 2 based on the GLORYS12 model compare to the OSNAP observations?

5. How does the overturning strength vary per segment along the boundary currents of the SPG, for the long-term mean and on interannual and seasonal timescales?

With these research questions (RQ) in mind, a methodology is set up (section 3). The reanalysis model GLORYS12 is used (sections 3.a) to calculate the overturning strength. The SPG is first split up into sub-basins to determine the overturning over large-scale areas (RQ 1, section 4.a). The seasonal (RQ 2) and interannual (RQ 3) variability are investigated and explored (section 4.a). The comparison with OSNAP is done in section 4.b. Next, the SPG is subdivided into seventeen segments (section 4.c). These segments cover a small part of the boundary currents in the SPG, to further analyze where the overturning takes place exactly. Again, the seasonal and interannual overturning are investigated. Finally, the findings and results will be discussed in section 5.

# 3 Data & Methodology

In this chapter, the data and methodology are explained. First, the GLORYS12 model is used as the data source in this study (section 3.a). Next, the density calculation and classification of the ocean is explained in section 3.b, which is needed to determine the overturning in density space. This is followed by the overturning calculations in density space (section 3.c). Finally, the spatial scales (section 3.d) and temporal scales (section 3.e) studied are motivated and explained.

## 3.a GLORYS12 model

To investigate the overturning in the SPG, a reanalysis model is chosen. This allows for a detailed study of the overturning in the past, with no limitations to specific locations of observations. A part of the overturning depends on eddy activity along the boundary currents of the SPG (section 2.c). Therefore, an eddy-resolving high spatial resolution model is needed, to simulate the overturning accurately. The GLORYS12 model is chosen to use, with its high eddy-resolving capabilities. The model is best described by Jean-Michel et al. (2021): "GLORYS12 is a global eddy-resolving physical ocean and sea ice reanalysis at 1/12°horizontal resolution covering the 1993-present altimetry period, designed and implemented in the framework of the Copernicus Marine Environment Monitoring Service (CMEMS)." The model is forced by the atmospheric reanalysis from the European Center for Medium-Range Weather Forecasts. Next to that, GLORYS12 uses satellite altimetry and in-situ observations for data assimilation. It should be noted the OSNAP data is not included in this, so it can be used as independent observations to validate results. The model's output is in a daily frequency from 1993 to 2020. This allows the results to be compared to the OSNAP observations (section 2.a) from 2014-2020. This study uses the horizontal velocity, temperature, and salinity to determine the overturning strength in the SPG (section 3.c).

The model has a quasi-isotropic horizontal grid with a 1/12° resolution between 4 and 5 kilometres in the SPG area, depending on latitude. The high spatial resolution enables the model to simulate mesoscale eddies, essential for the overturning processes described in section 2.c. The vertical grid consists of fifty layers, with a thickness of 1-450 meters. The first 22 layers are in the top 100 meters. Therefore, the model has a high accuracy for the top 700 meters but the uncertainty increases below 700 meters (Verezemskaya et al., 2021). This study concludes the GLORYS12 model is still accurate down to 1000 meters, but between 1000-2000 meters the combination of higher layer thickness and less observational data to assimilate, Below 2000 meters there is almost no observational data, so some of the model biases are not accounted for here. Mainly, this results in the waters below 2000 meters being significantly warmer and saltier. The temperature bias is between 0.5°C and 1°C warmer and the salinity is between 0.03-0.05 g/kg higher, resulting in a decreased potential density of these waters of about 0.045-0.096 kg/m$^3$. This results in a lower density gradient in the deep waters compared to real life, increasing the potential overturning strength, because the mixed layer can reach deeper.

The model is based on the Navier-Stokes equations and nonlinear equation of state to couple temperature and salinity to the velocity (Madec et al., 2017). Additionally, it uses approximations, whereof the four most important ones are discussed. The Boussinesq approximation states that density variations are only considered for the buoyancy force and the hydrostatic approximation makes the vertical pressure gradient only dependent on the buoyancy force (1):

$$\frac{\partial p}{\partial z} = -\rho g; \qquad \rho = \rho(T, S, p) \tag{1}$$

where:

$\rho$ = Density [kg/m$^3$]
$T$ = Temperature [K]
$S$ = Salinity [g/kg]
$p$ = Pressure [Pa]

The density ($\rho$) can be determined by the equations of state, using six equations and unknowns ((UNESCO, 1991)).

The third approximation is the incompressibility of the water, which yields the divergence of the velocity vector U is assumed zero (2).

$$\nabla \cdot U = 0 \tag{2}$$

where:
$\nabla$ = generalised derivative vector operator in $(i, j, k)$ directions
$U$ = Velocity vector [m/s]

Then, by using the turbulent closure approximation, which parametrizes small-scale turbulent processes, the momentum balance can be defined:

$$\frac{\partial \mathrm{U}_h}{\partial t} = -\left[(\nabla \times \mathrm{U}) \times \mathrm{U} + \frac{1}{2}\nabla\left(\mathrm{U}^2\right)\right]_h - fk \times \mathrm{U}_h - \frac{1}{\rho_o}\nabla_h p + \mathrm{D}^{\mathrm{U}} + \mathrm{F}^{\mathrm{U}} \tag{3}$$

where:
$f$ = Coriolis paramater [1/s]
$U_h$ = Horizontal velocity vector [m/s]
$D^{\mathrm{U}}$ = Momentum small-physics forcing term [m/s$^2$]
$F^{\mathrm{U}}$ = Momentum surface forcing term [m/s$^2$]

The surface momentum force $\mathrm{F}^{\mathrm{U}}$ consists of the wind shear stress on the water. The small-physics momentum force $\mathrm{D}^{\mathrm{U}}$ is a parameterization of the turbulent forces in the water.

The mass conservation is build into two equations: heat conservation (4) and salt conservation (5).

$$\frac{\partial T}{\partial t} = -\nabla \cdot (T\mathrm{U}) + D^T + F^T \tag{4}$$

$$\frac{\partial S}{\partial t} = -\nabla \cdot (S\mathrm{U}) + D^S + F^S \tag{5}$$

where:
$T$ = Temperature [K]
$S$ = Salinity [g/kg]
$U$ = Velocity vector [m/s]
$D^{\mathrm{T}}$ = Heat small-physics forcing term [m/s$^2$]
$F^{\mathrm{T}}$ = Heat surface forcing term [m/s$^2$]
$D^{\mathrm{S}}$ = Salinity small-physics forcing term [m/s$^2$]
$F^{\mathrm{S}}$ = Salinity surface forcing term [m/s$^2$]

The heat surface forcing term ($F^{\mathrm{T}}$) is regulated by the heat exchange with the atmosphere. The salinity surface forcing term is regulated by precipitation and evaporation, where a surplus of precipitation yields a decrease in salinity. The heat and salinity small-physics forcing terms $\mathrm{D}^{\mathrm{T}}$ and $\mathrm{D}^{\mathrm{S}}$ are parameterizations of the effect of turbulence on the heat and salt balance.

The model's output consists of several variables with a daily output frequency, of which the following will be used in this study: potential temperature, salinity, and velocity in zonal and meridional directions.

## 3.b Creating density classes

To examine the overturning in the SPG, first density classes are created. These are classes defined by a minimum and maximum density and all water in between is considered part of the class. This enables an analysis of the change in transport per density class, from which the overturning strength can be determined (section 3.c).

The GLORYS12 model provides as output the temperature, salinity and horizontal velocity. The potential density $\rho_0$ is calculated, according to the equations of state (UNESCO, 1991). The potential density $\rho_0$ represents the water's density when raised adiabatically to the surface. This negates the influence of pressure on the density, allowing for an analysis in density space independent of depth. The potential density also ignores the effect of thermal and salt expansion pressure coefficients. This results in the potential density $\rho_0$ decreasing at great depths instead of increasing. This effect is notable below 3000 meters deep, which is not reached in the boundary currents of SPG. However, the Labrador Sea's interior reaches below 3000 meters, so a slightly higher potential density can be expected here. Therefore, the potential density $\rho_0$ is used, enabling a good analysis of the overturning in density space over all boundary currents in the SPG. Additionally, the OSNAP observations use the potential density $\rho_0$ to determine the overturning. Using the same density measures allows for a better comparison to the observations.

Typical values of $\rho_0$ are between 1027.0 and 1027.8 kg/m$^3$. Therefore, $\sigma_0$ is introduced, which is $\rho_0$ - 1000 kg/m$^3$. Next, the water column is divided into density classes ranging from $\sigma_0 = 27.00$ to $\sigma_0 = 27.80$ kg/m$^3$ with incremental steps of $\Delta\sigma_0 = 0.025$ kg/m$^3$. In figure 10 the density in the Iceland Basin is shown as an example. Here, every tint of blue represents a density class. As can be seen, the potential density ranges between 27.0 kg/m$^3$ (white) and 27.8 kg/$^3$ (dark blue).

In summary, ocean water is classified in density classes with $\Delta\sigma_0 = 0.025$ kg/m$^3$. This enables a detailed study of the overturning, using a mass balance, explained in section 3.c.

## 3.c Calculating the overturning in density space

This section explains how the overturning is determined within the GLORYS12 data. The overturning strength is calculated using a mass-balance as sketched in figure 11. Here, a segment along a boundary current is shown, with an inflow and outflow transport. The transport is divided into density classes (section 3.b) represented by the colored bars. The difference between inflow and outflow equals the transport difference over the segment, which can be attributed to the three different processes of overturning (section 2.c): Along-isopycnal transport (1), Shallow convection (2), and Overflows (3). This study focuses only on the overall overturning based on the outflow and inflow differences. The overturning strength calculation is explained step by step.

First, the transport of water ($Q_{\sigma_i}$) per density class ($\sigma_i$) at the in- and outflow is calculated (the two bar-plots on the left hand side of figure 11). Here, i=1 is the lowest density class at the surface. This is done according to equation (6):

$$Q_{\sigma_i}(u, v, A_{\sigma_i}) = \int [cos(\alpha)u(x, y) + cos(\beta)v(x, y)]dA_{\sigma_i} \tag{6}$$

where:

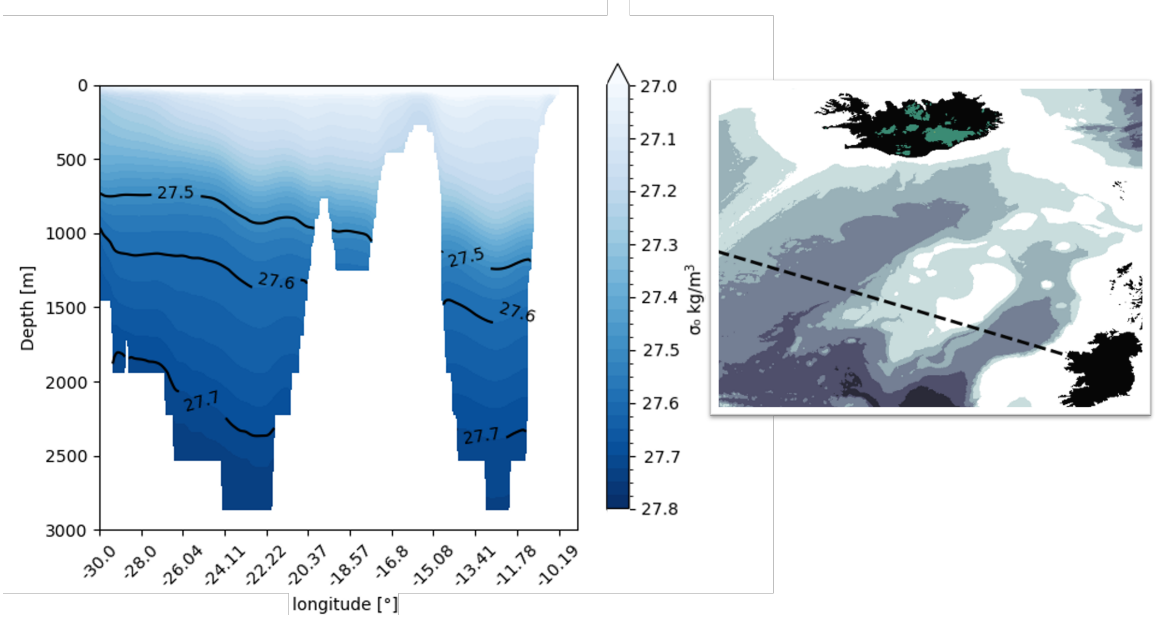


Figure 10: Cross-section of the Iceland Basin illustrating the defined density classes. The top right shows the exact location of the cross-section. Each tint of blue represents a density class with $\Delta\sigma_0$ = 0.025 kg/m$^3$, increasing with density with darker blue.

$\alpha$ = angle of the cross-section with the longitudinal direction [rad]
$\beta$ = angle of the cross-section with the latitudinal direction [rad]
$dA_{\sigma_i}$ = cross-sectional area of density class i [m$^2$]
$u(x, y)$ = daily mean velocity in latitudinal direction [m/s]
$v(x, y)$ = daily mean velocity in longitudinal direction [m/s]
$x$ = horizontal coordinate of cross-section [lat,lon]
$y$ = depth coordinate of cross-section [m]

Using equation (6) two cross-sections perpendicular to the flow direction of the boundary current are considered, one up- and one downstream. Together they are referred to as a segment. Now, the mass-balance of a segment is defined in (7):

$$\sum_i Q_{\sigma_i,down} - \sum_i Q_{\sigma_i,up} = \sum_i \Delta Q_{\sigma_i} \tag{7}$$

Next, the cumulative sum (cumsum) is taken of $\Delta Q_{\varrho_i}$ for all density classes (i) (equation 8).

$$cumsum_k = \sum_{i=1}^{k} \Delta Q_{\varrho_i} \tag{8}$$

where:
$cumsum_k$ = the cumulative transport difference up to density class k [Sv]
$\Delta Q_{\varrho_i}$ = the transport difference for density class i [Sv]

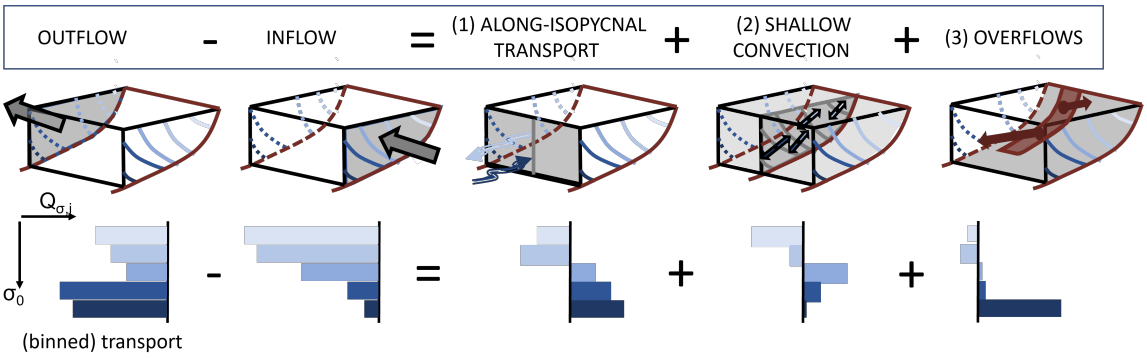


Figure 11: Schematic showing the mass-balance of a segment along a boundary current. The colored bars represent the transport per density class. The left side of the mass-balance is the difference between out- and inflow. The right side shows the contributions of each overturning process to the difference in transport along the segment (adapted from (Katsman, 2023)).

This allows for the identification and quantification of overturning. Figure 12b shows a sketch of the transport difference per density class in panel (a) and its respective cumulative transport in panel (b) over a segment. A negative (positive) transport difference indicates less (more) transport for that density class. The overturning is determined by the difference between the maximum and minimum of the negative slope ($NS_{i,max}$ and $NS_{i,min}$ respectively), indicated by the arrow in figure 12b.
In reality, the cumulative transport curve is not smooth, such as in figure 12b, but it has more noise. This results in multiple parts of the curve with a negative slope. Therefore, all parts with a negative slope are identified to calculate the total overturning. Next, their respective maximum ($NS_{i,max}$) and minimum ($NS_{i,min}$) values are determined and their sum is the total overturning (TO) (equation 9).

$$TO = \sum_i NS_{i,max} - NS_{i,min} \tag{9}$$

This equation 9 represents the total overturning between the up- and downstream sections over a segment. This is the main focus of this study. A more detailed study of the type of overturning is possible. To this end, $\Delta Q_{\sigma_i}$ can be split into three different components (figure 11): (1) along-isopycnal transport, (2) shallow convection, and (3) overflows (equation 10).

$$\sum \Delta Q_{\sigma_i} = \sum \Delta Q_{\sigma_i,(1)} + \sum \Delta Q_{\sigma_i,(2)} + \sum \Delta Q_{\sigma_i,(3)} \tag{10}$$

$Q_{\sigma_i,(1)}$ is determined with a cross-section along the boundary current, connecting the up- and downstream cross-sections. Here, the flow direction is positive into the segment. $Q_{\sigma_i,(3)}$ is similar, but the cross-section is taken along an overflow region. Figure 13 presents a schematic overview of the different cross-sections. Then, $Q_{\sigma_i,(2)}$ is assumed equal to the overall transport difference $\Delta Q_{\sigma_i}$ minus $Q_{\sigma_i,(1)}$ and $Q_{\sigma_i,(3)}$. The overturning strength for processes (1), (2) and (3) individually can be determined the same way as $Q_{\sigma_i}$, using equations (8) and (9). Some preliminary results of such a division of overturning processes are made in this study, but need to be further improved to give useful results.

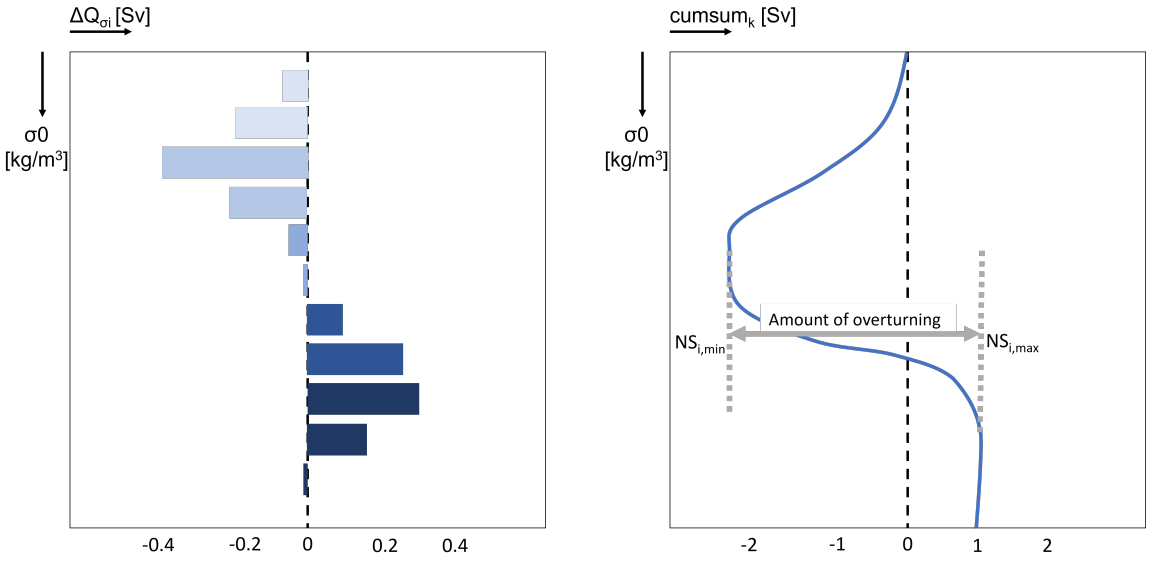


(a) (b)

Figure 12: This is an example of (a) the transport difference per density class $\Delta Q_{\sigma i}$ and (b) its respective cumulative transport difference $cumsum_k$ for a segment. The overturning strength can be quantified with the difference between the minimum and maximum values of the part of the curce with a negative slope.

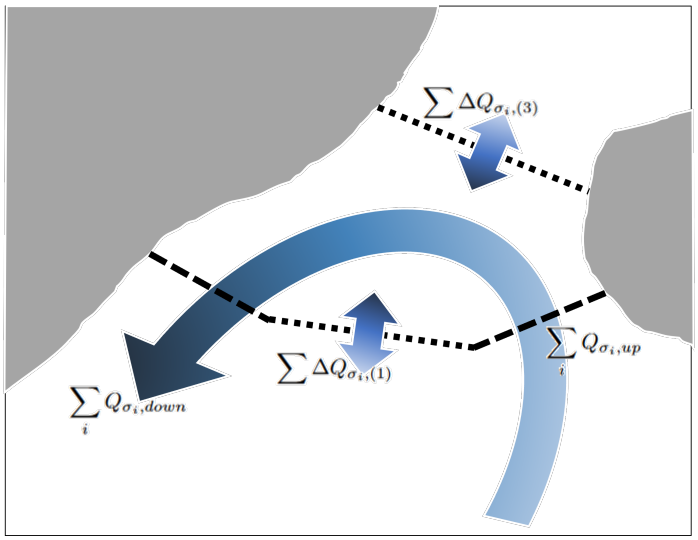


Figure 13: Schematic overview of the different cross-sections in a segment with their respective transports $\sum Q_{\sigma_i}$. The total overturning is determined by the difference in transport between the down- and upstream cross-sections (thick dashed lines). The northerly dotted line is the overflow cross-section and the lower one is the alongstream cross-section, with transports $\sum \Delta Q_{\sigma_i,(1)}$ and $\sum \Delta Q_{\sigma_i,(3)}$ respectively. They divide the total overturning into the different processes according to equation (10).

Summarizing, a segment of a boundary current is defined with an up- and downstream cross-section perpendicular to the flow direction. The transport per density class is calculated for both sections. The difference in transport between the up- and downstream sections per density class determines the overturning strength. The alongstream section, and overflow section if present, make it possible to determine the type of overturning, but this is not fully incorporated in this study. Next, this approach to analyze the overturning is applied on different spatial and temporal scales, explained in sections (3.d) and (3.e) respectively.

## 3.d Analyses on varying spatial scales

In this study, the overturning is 1) analyzed on the scales of the entire SPG, 2) its main ocean basins and 3) along smaller segments of the boundary current. Scale 1) and 2) are also compared to the OSNAP-observations, to see how the GLORYS12 model data compares to real data.

The basin-scale analysis focuses on the overall overturning in the SPG and how it is divided between the major basins. To start, the SPG is divided into three sub-basins. These are the Iceland basin, Irminger Sea, and Labrador Sea, schematized in figure 14. These basins are all characterized by the cyclonic current, described in section 2.b and shown with blue arrows in figure 14. The dashed black lines represent cross-sections over the full depth of the ocean. Next, the upstream, downstream and overflow cross sectional transports are defined for each basin.

- Iceland Basin:
  - $Q_{\sigma_i,up}$ = Iceland Basin (ICE)
  - $Q_{\sigma_i,down}$ = Reykjanes Ridge (RR)

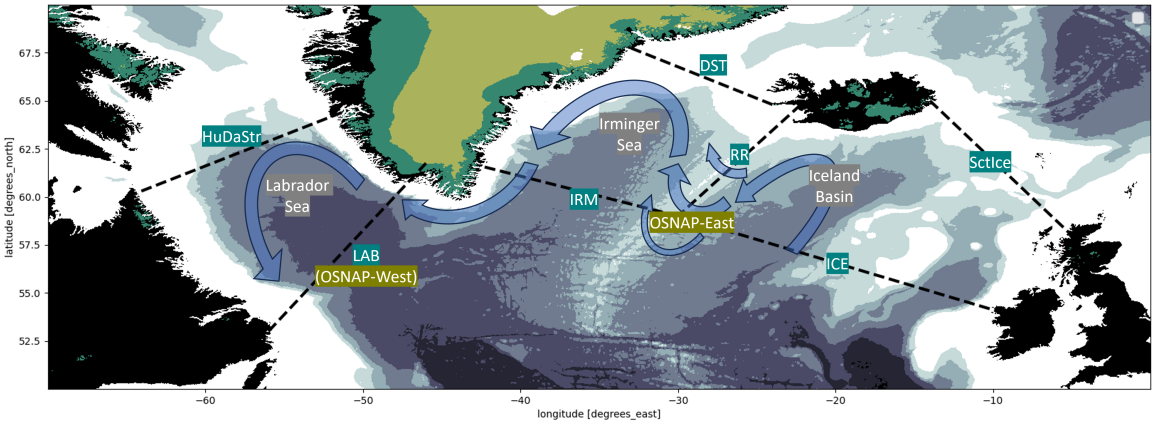


Figure 14: Schematic of the Sub-Basins in the SPG. Labrador Sea in the west, Irminger Sea in the middle and Iceland Basin in the east. The blue arrows represent the boundary currents in the SPG. ICE=Iceland, SctIce=Scotland-Iceland Ridge overflow, RR=Reykjanes Ridge, DST=Denmark Strait overflow, IRM=Irminger, LAB=Labrador, HuDaStr=Hudson-Davis Strait overflow. OSNAP-West is the same as LAB, OSNAP-East is IRM and ICE combined.

  - $Q_{\sigma_i,(3)}$ = Scotland-Iceland Ridge (SctIce)

- Irminger Sea:
  - $Q_{\sigma_i,up}$ = Reykjanes Ridge (RR)
  - $Q_{\sigma_i,down}$ = Irminger Sea (IRS)
  - $Q_{\sigma_i,(3)}$ = Denmark Strait (DS)

- Labrador Sea:
  - $Q_{\sigma_i,up}$ - $Q_{\sigma_i,down}$ = Labrador Sea (LAB)
  - $Q_{\sigma_i,(3)}$ = Hudson-Davis Strait (HuDaStr)

$Q_{\sigma_i,(1)}$ and $Q_{\sigma_i,(2)}$ can not be distinguished in the basin analysis, because there is no division made between the interior and boundary current of the basins. Next, the overturning can be determined using equations (7), (8) and (9). $Q_{\sigma_i,(3)}$ is used to determine the contributions of overturning within the basins and the overflow regions.

The GLORYS12 results are validated using the OSNAP observations (section 1). OSNAP calculates the total overturning using the same approach as in this study. Their observations are situated over the Labrador Sea (LAB), Irminger Sea (IRM) and Iceland Basin (ICE) cross-sections from figure 14. OSNAP divides the SPG in East and West, with the ICE and IRM cross-sections combined as East, because they do not have observations along the Reykjanes Ridge (Fu et al., 2023; de Jong et al., 2020)). The overturning strength is then calculated using the difference between poleward transport ($Q_{\sigma_i,up}$) and equatorward transport ($Q_{\sigma_i,down}$).

Finally, the boundary currents in the SPG are divided into seventeen smaller segments (figure 15). The segments are numbered from zero to sixteen, increasing in downstream direction.
For each segment, an up- down and alongstream cross-section is defined, with $\sum Q_{\sigma_i,up}$, $\sum Q_{\sigma_i,down}$ and $\sum Q_{\sigma_i,(1)}$ the total transports respectively (figure 13). Segments 7 and 14 also have a non-zero

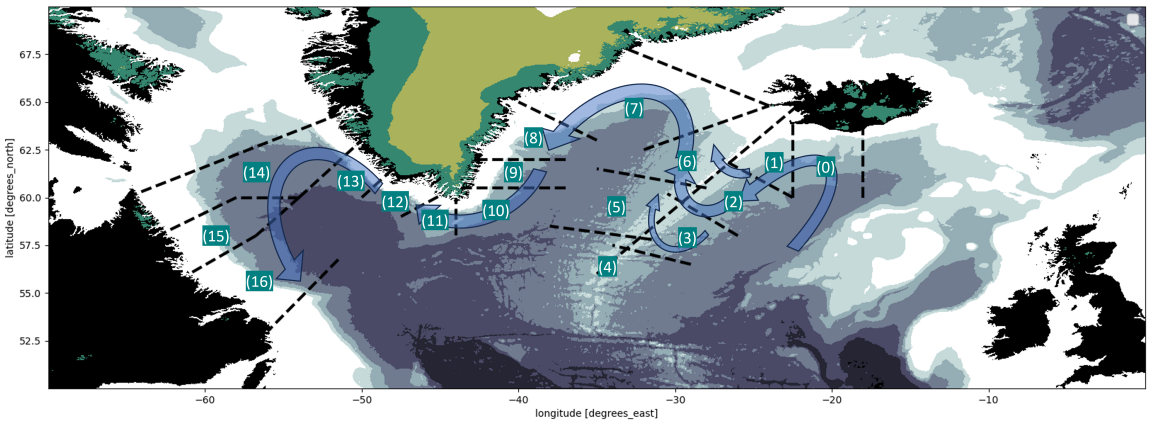


Figure 15: Schematic overview of the segments, numbered 0-16. The blue arrows represent the boundary currents.

$\sum Q_{\sigma_i,3}$ from the Denmark Strait and Hudson-Davis Strait respectively. The boundary current flows along the edges of the basins. In the Iceland Basin and the Irminger Sea the boundary current reaches down to the 2000 meter isobath (depth contour of the ocean floor) and in the deeper Labrador Sea down to the 3000 meter isobath on average. Therefore, the cross-sections in the respective basins are taken down to the 2000 or 3000 meter isobath.

The overturning strength does not include the density classes over which the overturning occurs. This results in a difference between the overturning strength of the entire SPG and the overturning strength of the basins combined or the basins compared to the segments combined, although enveloping the same area. Figure 16 exemplifies this discrepancy. Here, an overturning strength of 10 Sv in the Iceland Basin (figure 16a) and 10 Sv in the Irminger Sea (figure 16b) are combined still 10 Sv (figure 16c). What does change is the density range of overturning. The Iceland-Basin overturns low-density water into medium-density water, and the Irminger Sea overturns the medium-density water into high-density water. Combining both results in an overturning from low density to high density, but there is no increase in the overturning strength.

In summary, the overturning strength will be determined for the entire SPG, its basins and smaller segments along the boundary current. The GLORYS12 results are compared to the OSNAP observations for validation, using the same approach.

## 3.e Analysis on varying temporal scales

The analysis is not only done on different spatial scales, but also on different temporal scales. This section explains how the data is divided into mean annual and mean monthly overturning strength, to determine the inter-annual and seasonal dependencies of the overturning.

The temporal resolution of the GLORYS12 model is daily and ranges from 1993 to 2020. The output of the model is as daily mean values. Because $\sigma_0$ and $u$ and $v$ in equation (6) are highly variable, the overturning is calculated on the daily frequency. The daily overturning strength can then be averaged over longer periods of time. The annual overturning strength is the mean of all days of the year for every year from 1993-2020. From this, a possible linear trend is determined to

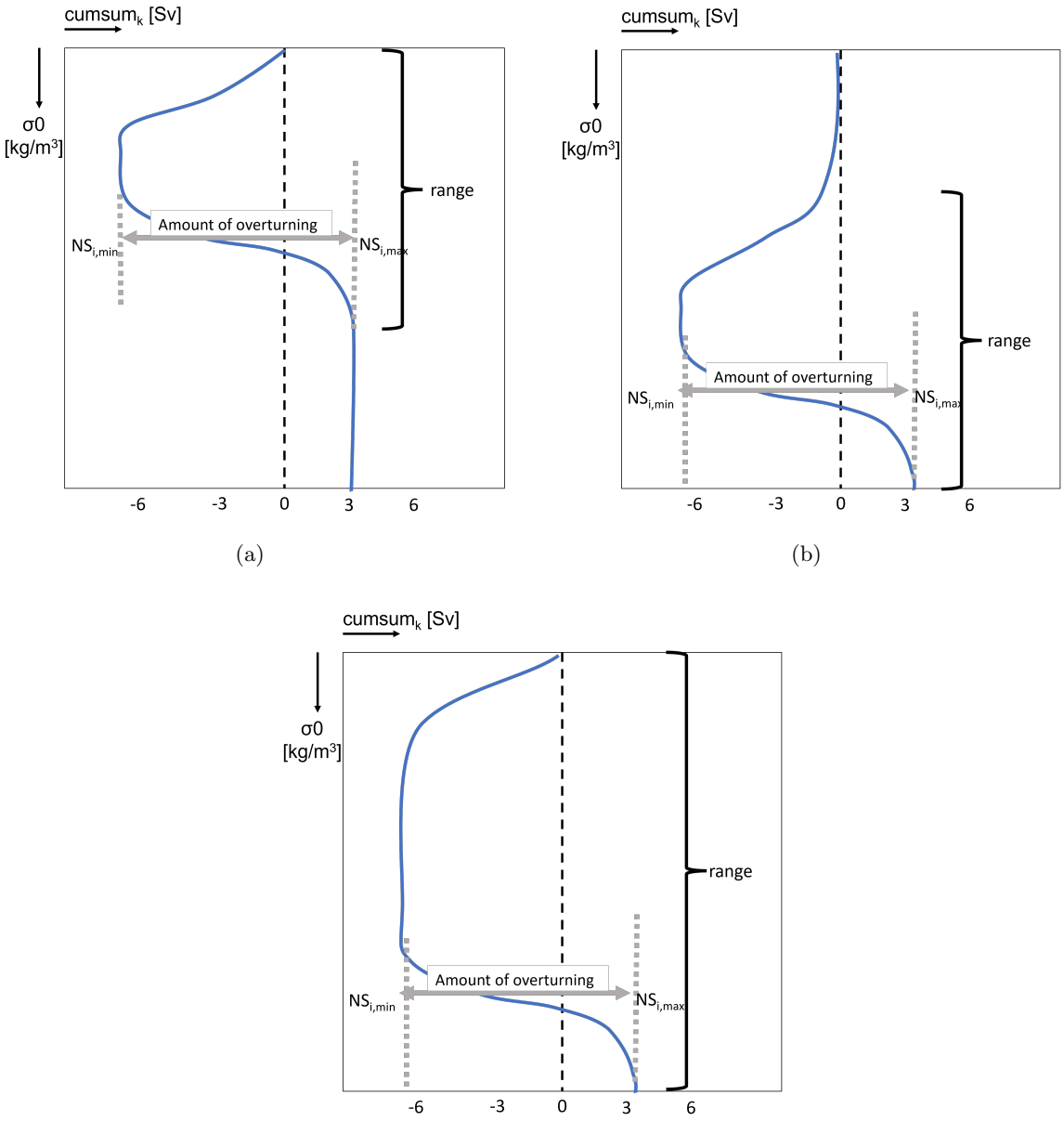


Figure 16: An example for how the sum of the overturning strength of basins or segments individually does not equal the total overturning strength of the basins or segments combined. (a) and (b) are examples of the cumulative transport difference of the Iceland Basin and Irminger Sea respectively. The overturning strength of both basins is 10 Sv (difference between the minimum and maximum of the negative slope (NS)). (c) shows the cumulative transport of both basins combined, with the same overturning strength and a large density range.

investigate if the inter-annual variation increases or decreases over the period.

The monthly overturning strength is the mean of all days of each month of every year from 1993 to 2020. The monthly overturning strength is reported with the standard deviation, to determine how large the variations of the overturning are. The same is done for the OSNAP validation, but for a time span of 2014-2020, corresponding to the same years as the latest OSNAP observations (Fu et al., 2023). In this paper, Fu et al. (2023) present the seasonal dependency of the overturning strength from observations, which is compared to the seasonal dependency of the GLORYS12 data.

To summarize, using the GLORYS12 reanalysis model, the overturning strength for the major basins and seventeen segments within the SPG is determined, using a mass balance principle. The overturning strength is analyzed on a inter-annual and seasonal basis, and is validated using the OSNAP-observations. Strong year and weak years can be identified to determine if the overturning the basins and segments have the same patterns. In section 4 the analysis results are presented and section 5 presents the conclusions and discusses the results, answering the research questions, finalized with recommendations for future research.

# 4 Overturning in the Sub-Polar Gyre

Within this study the overturning in the SPG is first determined over the entire area. In section 4.a the focus on the inter-annual and seasonal variations of the SPG. The SPG is subdivided into three sub-basins: the Labrador Sea, Irminger Sea and Iceland Basin to investigate if there are differences on a large scale between the west, middle and east of the SPG. The seasonal patterns and inter-annual variability are investigated between 1993-2020. The model is then compared with the OSNAP observations, using the time span 2014-2020, to make the connection to observational data (section 4.b). Here, the focus is to find the differences and similarities between the GLORYS12 model and real observations on a seasonal and inter-annual timescale. Next, the boundary currents of the SPG are divided in seventeen segments (section 4.c), to go into further detail on the spatial variation of the overturning strength along the boundary current of the SPG.

## 4.a Basin-scale Overturning

In this section, the long-term inter-annual and seasonal variability of the major basins in SPG are investigated over the time period 1993-2020. Here, the results are presented and a brief conclusion is given afterwards.

First, the SPG is divided into three basins (fig: 14): The Iceland Basin in the east, the Irminger Sea in the center and the Labrador Sea in the west. The inter-annual and monthly mean overturning strength for each basin is shown in figure 17a and 17b respectively. The mean overturning strength over the entire SPG is 23.8 Sv. The major basins have a strength of 16.6, 11.9 and 12.1 Sv, for the Iceland Basin, Irminger Sea, and Labrador Sea respectively. The total mean does not equal the sum of the basin means, because the overturning strength is determined without considering over which density classes (section 3.d).

For the annual mean overturning strength (fig 17a), there is a clear difference in overturning strength between the Iceland Basin and the other two basins. First, the mean overturning strength is 1.4 times stronger in the Iceland Basin compared to the Irminger and Labrador Sea. Also, the basins have differing long-term trends. The long-term mean overturning strength in the Iceland Basin is declining, with a linear trend of -0.04 Sv/year, the Irminger Sea with -0.02 Sv/year, and the Labrador Sea increases with 0.02 Sv/year. This results in a decrease of 1.12 and 0.56 Sv and an increase of 0.56 Sv between 1993 and 2020 respectively. This is not significant and well within the standard deviation of the basins. A more extended time period is needed to draw decisive conclusions on longterm trends and the variability.

Next, the monthly mean overturning results are shown in figure 17b. The Iceland basin shows a strong seasonal cycle, with a seasonal variation of 7.8 Sv between the peak in March and the minimum in September. The Irminger Sea's seasonal cycle is shifted one month earlier, with the peak in February and the minimum in August, and its variation is lower at 5.9 Sv. However, the relative seasonal variation is almost the same, with 47% and 49% variation compared to the mean for the Iceland basin and Irminger Sea respectively. The Labrador Sea has a significantly weaker seasonal variation of 3.1 Sv, which is 26% relative to its mean. Additionally, the seasonal cycle is shifted by another month earlier, compared to the Irminger Sea, with the peak in January and the minimum in June. Lastly, the standard deviation (shaded colors in figure 17) of the mean overturning strength over the time period 1993-2020 relatively is 10%, 12% and 17% of its mean for the Iceland Basin, Irminger and Labrador Sea respectively. So, the standard deviation of the overturning strength increases in the western direction.

The overturning strength does not consider over which density classes the overturning takes place. Therefore, the cumulative transport difference (equation 8) of each basin is further analyzed

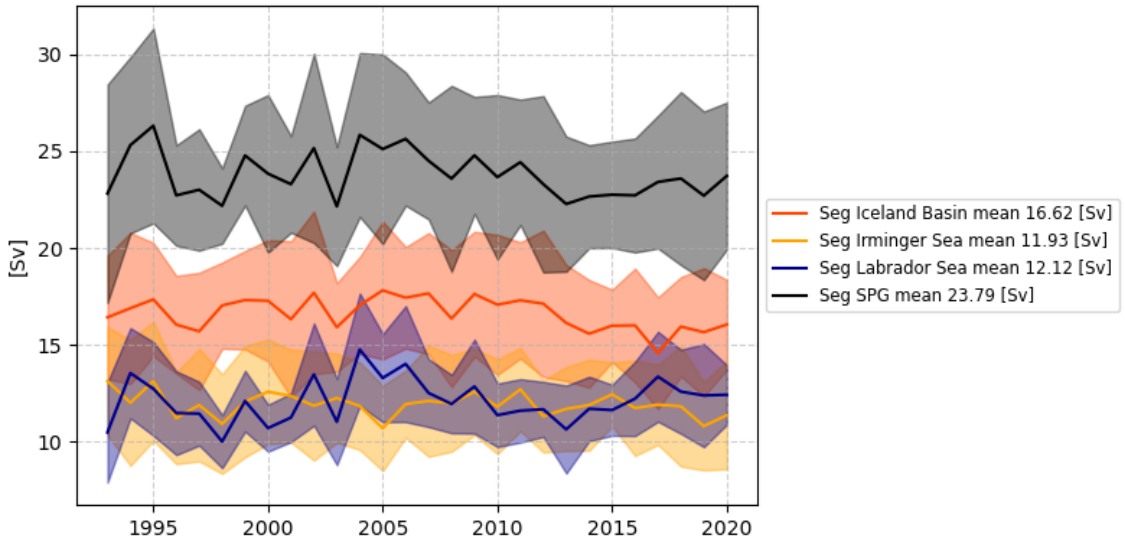


(a)

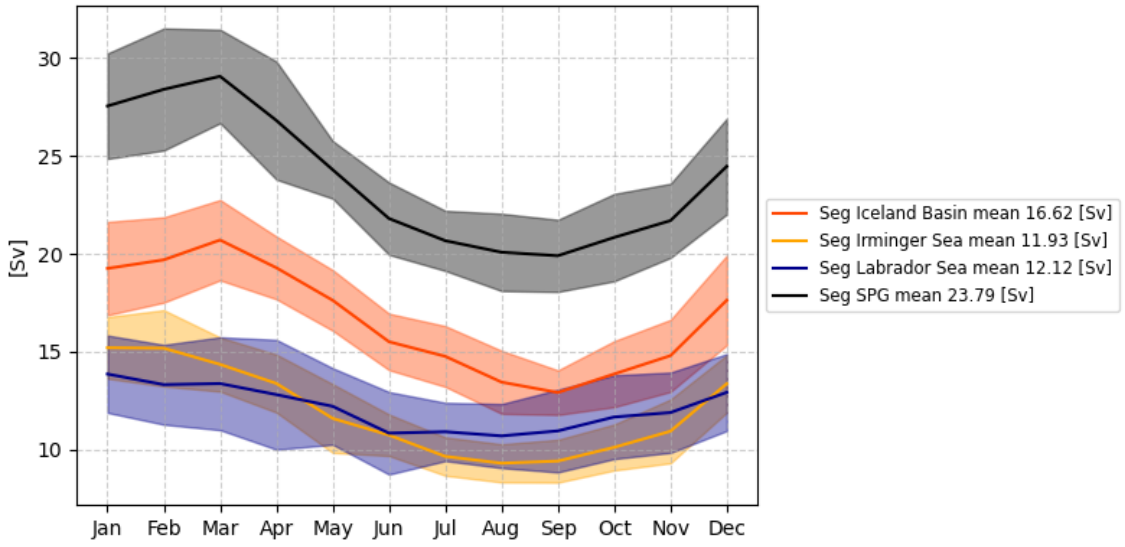


(b)

Figure 17: (a) The annual mean overturning strength and (b) the monthly mean overutrning strength for the Iceland Basin (red), Irminger Sea (orange), Labrador Sea (blue) and the total SPG (grey). Their respective overall mean overturning values are given in the legend. The shaded areas represent the standard deviation.

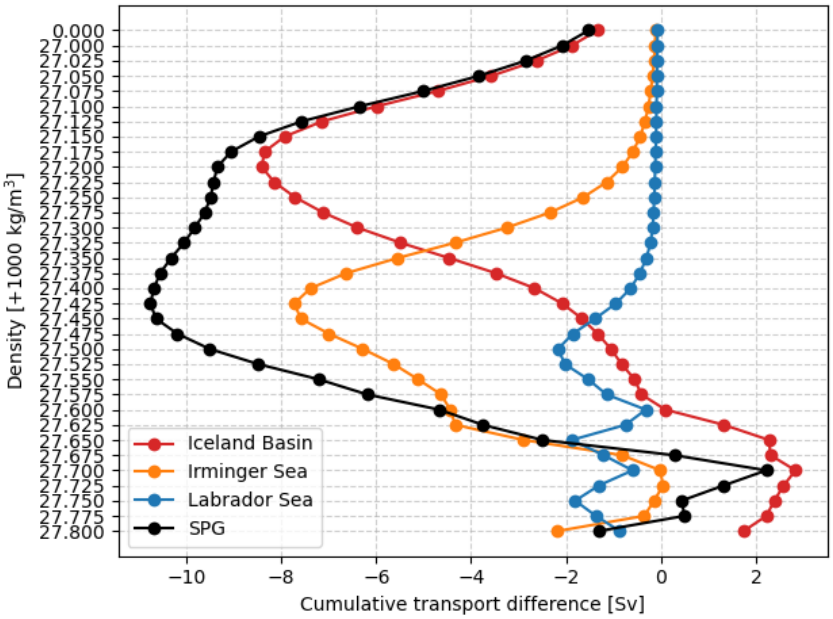


Figure 18: Cumulative transport difference of the Iceland Basin (red), Irminger Sea (orange), Labrador Sea (blue) and total SPG (black).

(fig 18). Figure 18 shows the mean cumulative transport difference of the time range 1993-2020.

The Iceland Basin has two overturning peaks. The first peak has a density range of $\sigma_0 = 27.0 - 27.55$ kg/m$^3$. This is predominantly due to shallow convection at the surface where the lowest density waters are present. The second peak has a density range of $\sigma_0 = 27.55 - 27.675$ kg/m$^3$. This increase can be attributed to the overflow from the Scotland-Iceland ridge, which introduces dense water to the basin.

The Irminger Sea (orange) has a similar pattern compared to the Iceland Basin, but the overall density of overturning increases. The first overturning peak has a density range of $\sigma_0 = 27.10 - 27.625$ kg/m$^3$, which again is mostly shallow convection. The second peak has a density range of $\sigma_0 = 27.625 - 27.725$ kg/m$^3$, which is overflow water from the Denmark Strait. These similarities signify both basins have similar overturning characteristics.

The Labrador Sea (blue) has a different pattern with three overturning peaks. The first ($\sigma_0 = 27.30 - 27.60$ kg/m$^3$) is again mostly shallow convection. The second ($\sigma_0 = 27.60 - 27.70$ kg/m$^3$) and third peak ($\sigma_0 = 27.70 - 27.80$ kg/m$^3$) are both most likely deep convection in the interior of the basin. The overflow from the Hudson-Davis Strait is mostly an exchange of low density fresh waters and does not contain very dense water. This signifies the difference between the Labrador Sea and the other two basins, with relatively more overturning over higher density classes, indicating there is not only shallow convection but also deep convection.

Overall, the three basins have a large inter-annual overturning strength variation and small linear trends can be determined, but an extended time period is needed for decisive conclusions. The seasonal cycle of the basins, combined with the density range of overturning, reveal some differences and similarities between the basins. The Iceland Basin and Irminger Sea have a similar seasonal overturning variation (figure 17b). Additionally, they have a similar cumulative transport difference

curve (18), although the Irminger Sea's curve is shifted downward to higher density classes. The Iceland Basin has an inflow of relatively warm surface waters from the North Atlantic Current (red arrows figure 4), which can be overturned by the cold atmosphere through shallow convection, due to the large temperature difference between the atmosphere and water. The Irminger Sea has the same situation, where the Irminger Current (light red arrow figure 4) still has relatively warm surface waters and shallow convection is again the dominating overturning process. In the Labrador Sea, this is less prominent, because the light surface currents consist mostly of fresh melt water (green arrows figure 4). This is cold water, close to freezing, so the temperature difference with the atmosphere in winter is lower compared to the eastern part of the SPG, reducing the potential shallow convection. Deep convection in the interior and lateral transport to the basins' interior is more variable than shallow convection and most likely contributes less to the overall overturning strength. Eddies are needed to transport water from the boundary current to the interior, which are not always present. Additionally, a deep mixed layer is required, which occurs with very cold atmospheric conditions, mostly in winter and early spring. The standard deviation of the Labrador Sea is highest in April (shaded blue area in figure 17b), which has a high chance of having the conditions for deep convection, indicating the high variability of deep convection. Further investigation of the differences and similarities between the basins is done in section 4.c, where the overturning along the boundary current is analyzed, using small segments. But first, the GLORYS12 is compared to the OSNAP observations in section 4.b.

## 4.b GLORYS12 compared to OSNAP

Next, the GLORYS12 data is compared to the OSNAP data. This is used to validate the GLORYS12 results, since the OSNAP observations are independent of the GLORYS12 model. For this, the SPG is divided in east (ICE and IRM) and west (LAB) (figure 14) and the time period of 2014-2020 is used. Figure 19 shows the seasonal variability of the GLORYS12 data (figure 19a) and the OSNAP observations (figure 19b), following RQ 4 (2.d).
The OSNAP total overturning strength peaks in May at 21.1 Sv and has its minimum in December with 12.3 Sv. In GLORYS12 the total overturning peaks in March at 29.1 Sv and has its minimum in August at 19.9 Sv. So, the seasonal variation for OSNAP (8.8 Sv) is very similar to GLORYS12 (9.1 Sv), but the peak overturning strength is shifted from May to March for GLORYS12.

The east for GLORYS12 and OSNAP has a similar seasonal variation of 5.9 and 6.1 Sv and the mean overturning strength is also similar with 17.6 and 17.0 Sv respectively. The west is 3 times stronger in GLORYS12 compared to OSNAP, with a mean of 12.6 Sv and 4.0 Sv respectively. The relative seasonal variation is stronger in OSNAP with 60% compared to 40% for GLORYS12. This could be due to the large depths of the Labrador Sea. The GLORYS12 models' accuracy is lower below 2000 meters depth 3.a and a negative bias occurs for the highest densities, resulting in less dense deep waters. This can result in a higher overturning strength than reality, because part of the overturning takes place below 2000 meters in the Labrador Sea.

A major difference between OSNAP and GLORYS12, is that OSNAP is based on observations that are almost exclusively in the boundary currents. In contrast, GLORYS12 provides data over the entire basin, including the interior. The water in the interiors of the basins do not have a zero velocity. Therefore, a part of the overturning can occur within the interior itself, without transport exchange with the boundary current. The seasonal shift may also be due to the extended data for the interior of the basins in GLORYS12. The extra overturning that occurs here, might have a quicker reaction to a colder atmosphere, and therefore shifting the seasonal cycle to earlier in the year. Further investigation on this is presented in the next section, where the overturning along the boundary current is analyzed, using small segments.

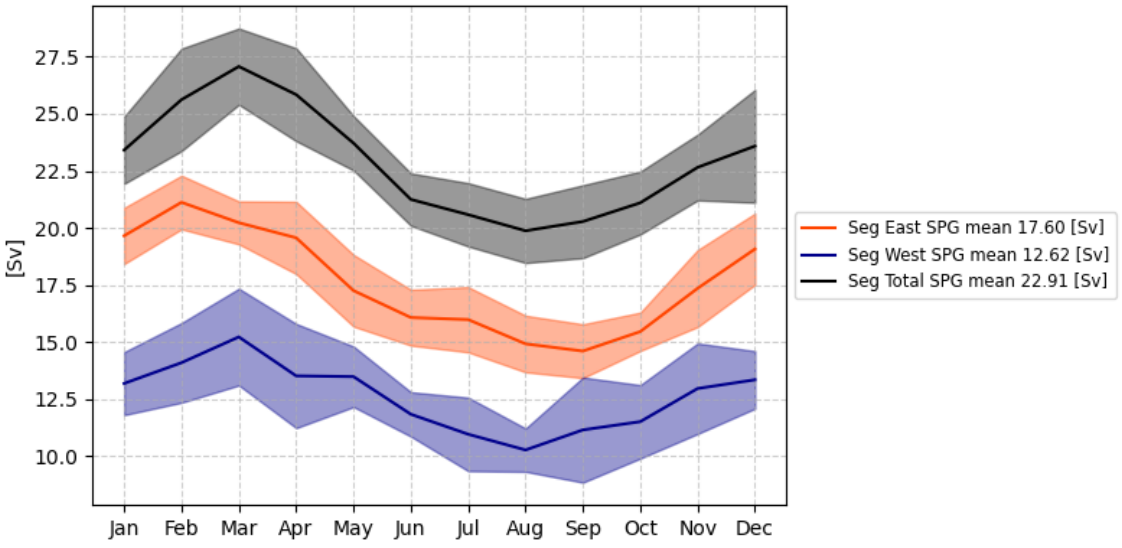


(a)

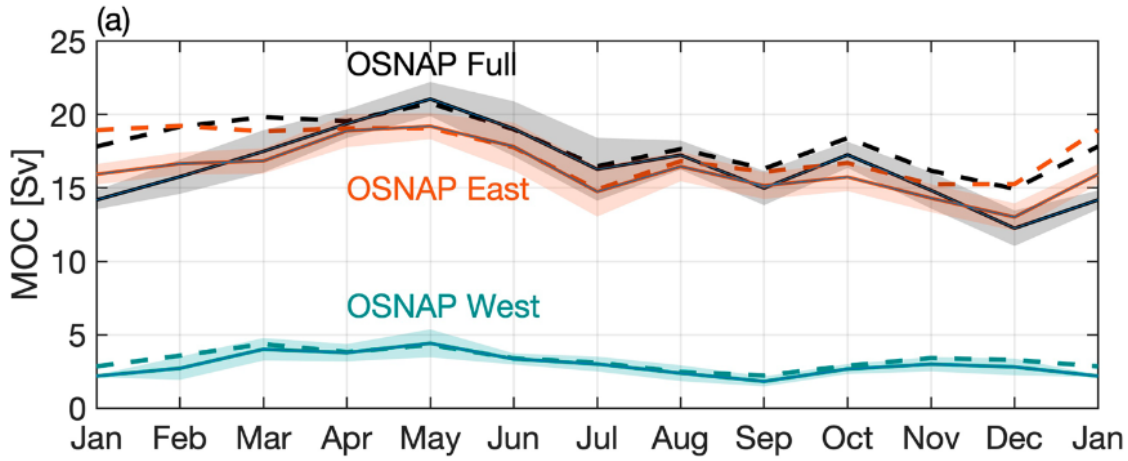


(b)

.

Figure 19: The seasonal variation in overturning strength in (red) East SPG, (blue) West SPG and (black) total SPG, for (a) GLORYS12 data and (b) OSNAP data over the period 2014-2020 (Fu et al., 2023).

## 4.c Overturning along segments of the boundary current

Seventeen segments along the boundary current are defined (figure 11) and each segment's inter-annual and seasonal variability of the overturning strength is examined. However, compared to the basin analysis, it became apparent that the difference between the in- and outflow of a segment can be significantly high: the mean difference in transport can be as high as 10 Sv. This discrepancy skews the overturning calculations to either overestimating overturning strength (downstream transport higher) or underestimating overturning strength (downstream transport lower). This problem is resolved by normalizing the transport at each segment before calculating the overturning strength, by dividing the transport for each by the total transport of the section and multiplying it by the average transport of the two sections. This results in the same average transport for both cross-sections. Using this, the overturning can be calculated, but it should be taken into account the outcome is not the real overturning of the segments. The contributions of the overturning within the boundary current and the overturning through offshore transport with the center of the basin can not be distinguished, when averaging the transport through a segment. However, an indication of the overall overturning strength can be made and over which density classes the overturning takes place.

The inter-annual variation of the overturning strength for each segment is presented in figure 20. The black line represents the annual mean overturning strength with its standard deviation in grey. The red dashed line is the linear trend, of which the trend value is given in the legend of each graph. The results show an overturning strength for each segment between 4.27 Sv (seg 9) and 9.13 Sv (seg 7). The sum of all segments' overturning strength is much higher than that of the basins combined. This is, again, because the overturning strength does not take into account over which density classes the overturning takes place, just as for the basins (section 4.a, figure 16). Almost all segments show an increasing linear trend, except for 2, 3 and 4 in the Iceland-Basin. The Iceland-Basin had the strongest decreasing trend in the basin analysis (section 4.a), so the decreasing trends here are expected. However, the Irminger Sea shows a completely opposite trend, with the basin having a -0.02 Sv/y trend and the segments having a 0.01 to 0.05 Sv/y trend. The Labrador does have positive trends for both the basin (0.02 Sv/y) and the segments (0.02 - 0.09 Sv/y), but the segments do have a stronger trend. These differences indicate the high spatial variability of the overturning in the SPG.

Most segments also have a seasonal cycle (figure 21), similar to the basins. The figure shows the monthly averaged overturning for each segment, with the seasonal variation relative to the mean (SV) and seasonal range (SR). The SV is the difference between the maximum and minimum monthly overturning strength divided by the overall mean of the segment. The SR is the months of maximum and minimum monthly overturning strength respectively. All segments have a seasonal cycle with a minimum SV of 32% of the mean overturning strength. The SV is stronger compared to the basins' and most segments have the maximum overturning in January, which is 2 months earlier than the basins. This indicates the overturning in the segments has relatively high shallow convection overturning compared to the basins, which is more seasonally dependent. However, the segments in the Iceland Basin ($\overline{SV} = 67\%$) and the Irminger Sea ($\overline{SV} = 63\%$) have a higher SV compared to the Labrador Sea ($\overline{SV} = 44\%$). Again, this indicates more shallow convection in the Iceland Basin and Irminger Sea just as for the basin analysis (section 4.a).

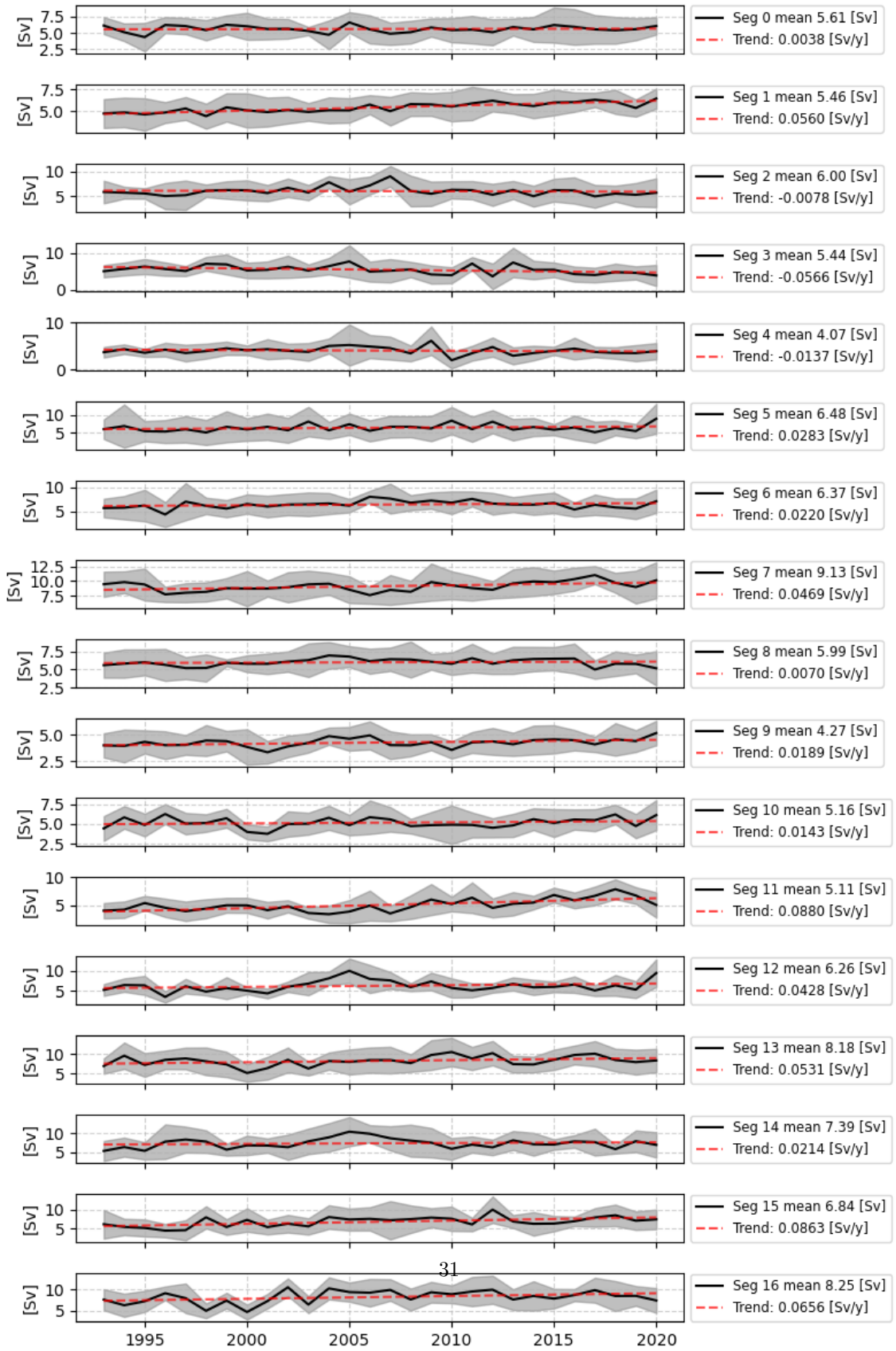


Figure 20: Annual overturning strength for all segments. Segments are numbered 0-16, as depicted in figure 15. The overturning strength is based on the mean transport in the segment.

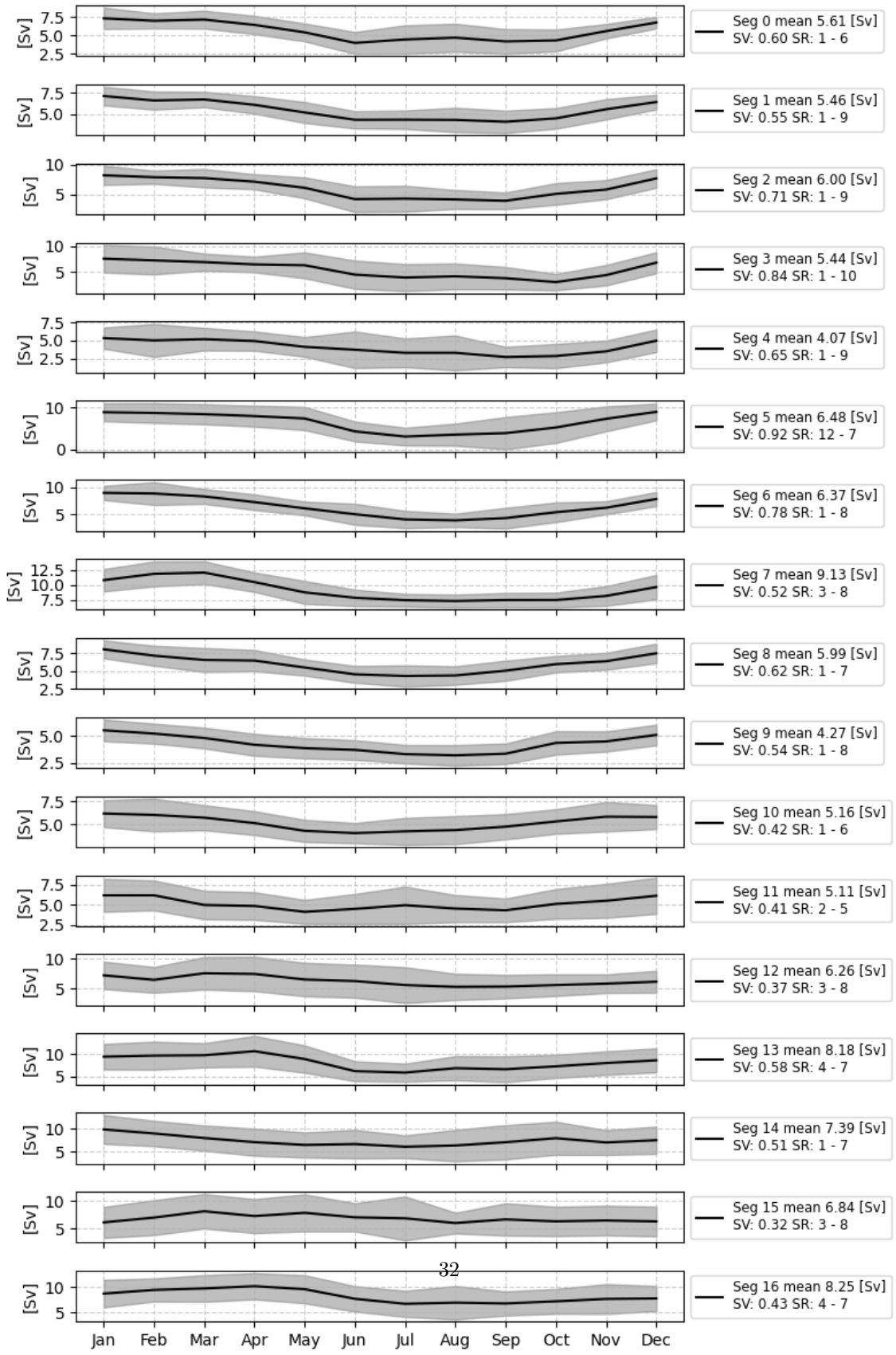




Figure 21: Monthly average overturning strength of the period 1993-2020 for all segments, numbered 0-16 as depicted in figure 15. On the y-axis is the overturning strength in Sverdrup and the x-axis are the months.

# 5 Conclusion & Discussion

This study has investigated the spatial and temporal variations of the overturning strength in the SPG, using the GLORYS12 reanalysis model.

First, the overturning strength of the three basins of the SPG was analyzed on an inter-annual and seasonal time scale (section 4.a). The mean overturning strength is 16.6 Sv, 11.9 Sv and 12.1 Sv in the Iceland Basin, Irminger Sea and Labrador Sea respectively. All three basins showed an inter-annual linear trend of -0.04, -0.02 and 0.02 Sv/year between 1993 and 2020 for the Iceland Basin, Irminger Sea and Labrador Sea respectively. These result in a change of -1.12 Sv, -0.56 Sv and +0.56 Sv in overturning strength over the entire time period of the basins respectively. This is still within the standard deviation of the basins and is therefore difficult to make predictions on the future trends of the overturning strength.

The basins share similarities in their seasonal overturning patterns, particularly the Iceland Basin and Irminger Sea, which exhibit comparable relative seasonal variations of 47% and 49% respectively. The Labrador Sea had a significantly lower relative seasonal variation of 26%. This difference is most likely due to the surface waters of the Labrador Sea being colder and partly melt water, resulting in a lower temperature difference between the atmosphere and water. This limits the potential shallow convection in the Labrador Sea during winter. The increased deep convection during winter is not able to compensate for the decrease in shallow convection.

The comparison with the OSNAP observations over the time period 2013-2020 showed a similar mean overturning strength (17.6 and 17.0 Sv) and seasonal variation (5.9 and 6.1 Sv) for the East SPG, but majorly differs for the West SPG (Labrador Sea). The Labrador Sea had a three times stronger mean overturning in the GLORYS12 model compared to the OSNAP observations from 2014 to 2020, with 12.6 Sv and 4.0 Sv.

A key distinction between OSNAP and GLORYS12 is the observational coverage of OSNAP. OSNAP primarily focuses on boundary currents, while GLORYS12 provides data spanning the entire basin, including the interior where water velocities are non-zero. This difference implies that some overturning may occur in the interior, without involving transport exchange with boundary currents. The additional overturning within the basin's interior might respond more quickly to colder atmospheric conditions, potentially leading to an earlier shift in the seasonal cycle.

Lastly, the segments of the boundary current showed a constant mean overturning strength between 1993-2020 along the boundary current. Overall, the inter-annual variability is similar for the basin scale overturning and segment scale overturning. However, the inter-annual linear trend of the segments of the Irminger Sea and the basin scale Irminger Sea did not correlate, where for the basin scale there is a decreasing trend of overturning strength, while the segments showed an increasing trend. This illustrates the high spatial variability of the overturning in the Irminger Sea.

The segment analysis is still only indicative of the overturning strength and its variability. Due to high spatial variability of the transport of the boundary current, the averaged transport in a segment is used. Further research could investigate the segments again, using the alongstream cross-section. This would enable an analysis of the overturning, without averaging transport, resulting in a more accurate overturning strength. In addition, using the alongstream cross-section, the overturning processes of shallow convection and deep convection can be further distinguished, to better analyze their independent temporal and spatial variability.

Overall, this study shows the overturning in the SPG is a highly variable process, with a high inter-annual variability, and it has a significant seasonal cycle that peaks in winter and declines in late summer and autumn everywhere in the SPG. This can be used to better model the overturning strength to increase the accuracy of future climate models.

# References


Bower, A., Lozier, S., Biastoch, A., Drouin, K., Foukal, N., Furey, H., Lankhorst, M., Rühs, S., and Zou, S. (2019). Lagrangian views of the pathways of the atlantic meridional overturning circulation.

Bras, I. A. A. L., Straneo, F., Holte, J., and Holliday, N. P. (2018). Seasonality of freshwater in the east greenland current system from 2014 to 2016. *Journal of Geophysical Research: Oceans*, 123:8828–8848.

Britannica, T. (2023). Thermohaline circulation. https://www.britannica.com/science/thermohaline-circulation retrieved on 13/04/2023.

Brüggemann, N. and Katsman, C. A. (2019). Dynamics of downwelling in an eddying marginal sea: Contrasting the eulerian and the isopycnal perspective. *Journal of Physical Oceanography*, 49:3017–3035.

Chafik, L., Holliday, N. P., Bacon, S., and Rossby, T. (2022). Irminger sea is the center of action for subpolar amoc variability. *Geophysical Research Letters*, 49.

Core Writing Team, H. Lee and J. Romero (eds.) (2023). *Climate Change 2023: Synthesis Report. Contribution of Working Groups I, II and III to the Sixth Assessment Report of the Intergovernmental Panel on Climate Change*. IPCC, Geneva, Switzerland.

Danek, C., Scholz, P., and Lohmann, G. (2023). Decadal variability of eddy temperature fluxes in the labrador sea. *Ocean Modelling*, 182:102170.

Daniault, N., Mercier, H., Lherminier, P., Sarafanov, A., Falina, A., Zunino, P., Pérez, F. F., Ríos, A. F., Ferron, B., Huck, T., Thierry, V., and Gladyshev, S. (2016). The northern north atlantic ocean mean circulation in the early 21st century. *Progress in Oceanography*, 146:142–158.

de Jong, M. F., de Steur, L., Fried, N., Bol, R., and Kritsotalakis, S. (2020). Year-round measurements of the irminger current: Variability of a two-core current system observed in 2014–2016. *Journal of Geophysical Research: Oceans*, 125.

Desbruyères, D. G., Sinha, B., McDonagh, E. L., Josey, S. A., Holliday, N. P., Smeed, D. A., New, A. L., Megann, A., and Moat, B. I. (2020). Importance of boundary processes for heat uptake in the subpolar north atlantic. *Journal of Geophysical Research: Oceans*, 125.

Fu, Y., Lozier, M. S., Biló, T. C., Bower, A. S., Cunningham, S. A., Cyr, F., de Jong, M. F., deYoung, B., Drysdale, L., Fraser, N., et al. (2023). Seasonality of the meridional overturning circulation in the subpolar north atlantic. *Communications earth & environment*, 4(1):181.

Georgiou, S., Ypma, S. L., Brüggemann, N., Sayol, J. M., van der Boog, C. G., Spence, P., Pietrzak, J. D., and Katsman, C. A. (2021). Direct and indirect pathways of convected water masses and their impacts on the overturning dynamics of the labrador sea. *Journal of Geophysical Research: Oceans*, 126.

Holliday, N. P., Bacon, S., Cunningham, S. A., Gary, S. F., Karstensen, J., King, B. A., Li, F., and Mcdonagh, E. L. (2018). Subpolar north atlantic overturning and gyre-scale circulation in the summers of 2014 and 2016. *Journal of Geophysical Research: Oceans*, 123:4538–4559.

Jean-Michel, L., Eric, G., Romain, B. B., Gilles, G., Angélique, M., Marie, D., Clément, B., Mathieu, H., Olivier, L. G., Charly, R., Tony, C., Charles-Emmanuel, T., Florent, G., Giovanni, R., Mounir, B., Yann, D., and Pierre-Yves, L. T. (2021). The copernicus global 1/12° oceanic and sea ice glorys12 reanalysis. *Frontiers in Earth Science*, 9.

Johnson, H. L., Cessi, P., Marshall, D. P., Schloesser, F., and Spall, M. A. (2019). Recent contributions of theory to our understanding of the atlantic meridional overturning circulation. *Journal of Geophysical Research: Oceans*, 124:5376–5399.

Jong, M. F. D., Aken, H. M. V., Våge, K., and Pickart, R. S. (2012). Convective mixing in the central irminger sea: 2002-2010. *Deep-Sea Research Part I: Oceanographic Research Papers*, 63:36–51.

Katsman, C. A. (2023). North atlantic cluedo: Controls on light upper ocean waters entering the deep ocean. *Application Form - NWO Open Competition Domain Science - M-1, 2022-2023*.

Koman, G., Johns, W. E., Houk, A., Houpert, L., and Li, F. (2022). Circulation and overturning in the eastern north atlantic subpolar gyre. *Progress in Oceanography*, 208.

Lozier, M. S., Bacon, S., Bower, A. S., Cunningham, S. A., Jong, M. F. D., Steur, L. D., Young, B. D., Fischer, J., Gary, S. F., Greenan, B. J., Heimbmbach, P., Holliday, N. P., Houpert, L., Inall, M. E., Johns, W. E., Johnson, H. L., Karstensen, J., Li, F., Lin, X., Mackay, N., Marshall, D. P., Mercier, H., Myers, P. G., Pickart, R. S., Pillar, H. R., Straneo, F., Thierry, V., Weller, R. A., Williams, R. G., Wilson, C., Yang, J., Zhao, J., and Zika, J. D. (2017). Overturning in the subpolar north atlantic program: A new international ocean observing system. *Bulletin of the American Meteorological Society*, 98:737–752.

Madec, G., Bourdallé-Badie, R., Bouttier, P.-A., Bricaud, C., Bruciaferri, D., Calvert, D., Chanut, J., Clementi, E., Coward, A., Delrosso, D., et al. (2017). Nemo ocean engine.

OSNAP (2023). A subpolar measure of the atlantic meridional overturning circulation. https://www.o-snap.org/. Accessed: 2023-11-23.

Paquin, J. P., Lu, Y., Higginson, S., Dupont, F., and Garric, G. (2016). Modelled variations of deep convection in the irminger sea during 2003-10. *Journal of Physical Oceanography*, 46:179–196.

Roussenov, V. M., Williams, R. G., Lozier, M. S., Holliday, N. P., and Smith, D. M. (2022). Historical reconstruction of subpolar north atlantic overturning and its relationship to density. *Journal of Geophysical Research: Oceans*, 127.

Stewart, R. H. (2008). Introduction to physical oceanography.

UNESCO (1991). Processing of océanographie station data. ISBN: 978-92-3-102756-792-3-102756-5.

Verezemskaya, P., Barnier, B., Gulev, S. K., Gladyshev, S., Molines, J. M., Gladyshev, V., Lellouche, J. M., and Gavrikov, A. (2021). *Journal of Geophysical Research: Oceans*, 126.